

Hints of BSM Higgs interactions by the combination $(\kappa_V^2 - \kappa_{2V})$ in HHjj production at LHC

D. Domenech, G. García-Mir, M. Herrero

Departamento de Física Teórica and Instituto de Física Teórica, IFT-UAM/CSIC,
Universidad Autónoma de Madrid, Cantoblanco, 28049 Madrid, Spain

E-mail: daniel.domenech@uam.es, guillermo.garciamir@estudiante.uam.es,
maria.herrero@uam.es

Abstract. In this work, we study the potential of analyzing the particular combination of κ modifiers given by $\kappa_V^2 - \kappa_{2V}$ to disentangle Beyond Standard Model Higgs signals in double Higgs production with two extra light jets at LHC. We use the Higgs Effective Field Theory approach, HEFT, for the gauge invariant description of these two κ_V and κ_{2V} parameters representing the BSM interactions of the Higgs particle with the electroweak gauge bosons, HVV and $HHVV$ respectively. We illustrate the bonus of studying this particular combination $\kappa_V^2 - \kappa_{2V}$ focusing in just one process, $HHjj$, instead of studying κ_V and κ_{2V} separately using various processes. For the detailed analysis here, we focus on the particular final state $H(\rightarrow \gamma\gamma)H(\rightarrow b\bar{b})jj'$, with two photons, two b-jets and two light jets, which we analyze fully including parton showering, fragmentation, hadronization and detector effects, in both signal and main background. We find that the sensitivity to $\kappa_V^2 - \kappa_{2V}$ could be notably improved at the HL-LHC by the proper cuts on the final state $b\bar{b}\gamma\gamma jj'$ that select optimally the events with VBF-topology and HH -topology. In particular, we propose strategies based on a good isolation of $\gamma\gamma$ and b-jet pairs, and focus specially on specific variables like $\eta_{\gamma\gamma}$ and $P_{\gamma\gamma}^T$ where the signal events distributions may discriminate efficiently between BSM signal versus SM background. We will show here how the high transversality of these two pairs in the signal (inherited from the high transversality of the H 's) is correlated with the non-vanishing value of this $(\kappa_V^2 - \kappa_{2V})$ combination.

Contents

1	Introduction	1
2	HVV and $HHVV$ interactions within HEFT: relation to the κ-formalism	4
3	The role of $(\kappa_V^2 - \kappa_{2V})$ in Higgs pair production from VBF	6
4	Exploring $HHjj$ production in pp collisions within HEFT	9
4.1	Vector Boson Fusion (VBF): Events selection strategy	9
4.2	HEFT total cross section, $\sigma(pp \rightarrow HHjj')$, versus $(\kappa_V^2 - \kappa_{2V})$	12
4.3	HEFT differential cross section, $d\sigma(pp \rightarrow HHjj')/d\eta_H$, versus $(\kappa_V^2 - \kappa_{2V})$	16
5	Detector-level HEFT prospects for $pp \rightarrow HHjj \rightarrow b\bar{b}\gamma jj'$	18
5.1	Detector-level SM prospects for the $b\bar{b}\gamma jj'$ final state	18
5.2	Detector-level BSM prospects within the HEFT for the $b\bar{b}\gamma jj'$ final state	20
6	Sensitivity to $(\kappa_V^2 - \kappa_{2V})$ in $b\bar{b}\gamma jj'$ events from $HHjj$ production at HL-LHC	26
	Conclusions	32
A	Feynman diagrams for double Higgs production in hadronic collisions	

1 Introduction

At present, due to the absence of any experimental signal of new particles or resonances beyond the Standard Model (SM) particle content, the main searches of Beyond Standard Model (BSM) physics are focused on the study of anomalous couplings of the SM particles and their phenomenological consequences at colliders. For that purpose, the use of κ coupling modifiers to analyze BSM Higgs physics at the Large Hadron Collider (LHC) has been widely explored in the past years. For summaries in joint reports see, for instance, Refs. [1–5]. Due to their relevance in connection with the Higgs mechanism of mass generation, among the most frequently studied BSM couplings are those describing new Higgs interactions with the electroweak (EW) gauge bosons $V = W^\pm, Z$. These BSM Higgs couplings are usually parametrized in terms of two modifiers κ_V and κ_{2V} , which refer to deviations to the HVV and $HHVV$ SM couplings, respectively. Both ATLAS and CMS collaborations have performed multiple searches at LHC, looking at different channels, and have provided a set of bounds on these κ parameters. A summary of the expected reach to the κ parameters in the future phase at LHC with $\sqrt{s} = 14$ TeV and high luminosity (HL-LHC) can be found in the recent joint paper by the ATLAS and CMS collaborations, Ref. [6].

On the computational side, the κ framework is not the common tool among the Theoretical Physics community, because in general this framework does not provide a full gauge invariant theory. In particular, to study BSM Higgs interactions, the usual framework adopted is that of Effective Field Theories (EFTs), which allow us to access these anomalous couplings under a gauge invariant and model-independent approach. On the other hand, the great advantage of EFTs is that they encode the low-energy limit of the particular high-energy “ultraviolet” (UV) physics model that one could be interested in. EFTs are usually built with effective Lagrangians by means of a tower of $SU(3)_C \times SU(2)_L \times U(1)_Y$ gauge invariant operators, with factors in front suppressed by inverse powers of the high energy scale or heavy

masses associated to the UV theory. These operators are built exclusively with the SM fields, and the coefficients in front (usually called Wilson coefficients) are the only ones encoding information about the underlying UV physics. In this respect, it is worth remarking that the usual procedure of setting the specific values for these coefficients by integrating out the heavy modes of the UV theory may also lead to interesting correlations among those coefficients. Then, EFTs are designed specifically to predict observable quantities being measured at colliders, with the hope of finally decoding the underlying physics operating at much higher energy scales. If the mentioned correlations can be tested at colliders, this will be a powerful tool to find hints of the new UV physics.

Currently, two of the most popular gauge invariant EFTs for describing BSM Higgs physics are the Standard Model Effective Field Theory (SMEFT) and the Higgs Effective Field Theory (HEFT) (for EFTs reviews see, for instance, Refs.[7, 8]). These two EFTs have linear and non-linear approaches, respectively, for the implementation of the Higgs Mechanism by means of the four scalar fields needed for the electroweak symmetry breaking $SU(2)_L \times U(1)_Y \rightarrow U(1)_{\text{em}}$, i.e. , the three would-be Goldstone bosons (GBs) and the Higgs field. In the SMEFT, these four fields are placed within a doublet, as in the SM, whereas in the HEFT, the Higgs field is a singlet and the three GBs are placed in a non-linear representation, usually in an exponential one. The present work is carried out using the HEFT, and, in particular, the HEFT model defined in [9–12]. The reason behind this choice is twofold. First, it provides an immediate connection with the κ framework. In particular, the Leading Order HEFT Lagrangian (LO-HEFT) with chiral dimension 2 contains two effective coefficients, usually named a and b , describing the effective interactions of our interest here, HVV and $HHVV$, which can be identified directly with κ_V and κ_{2V} , respectively. As a consequence, the experimental tests of these two HEFT effective coefficients, a and b , can be taken from those performed on their corresponding κ 's. One can always obtain the SM predictions from the general HEFT predictions by simply setting a and b to the reference values $a = 1$ and $b = 1$. Besides, since the HEFT is a fully gauge invariant theory, as said above, it provides gauge invariant predictions for all scattering amplitudes of phenomenological interest, which is not the case if one uses just a scaling of SM couplings by the κ 's. Second, and most importantly, due to the Higgs being a singlet within the HEFT, these two parameters a and b are independent and, therefore, provide generally uncorrelated HVV and $HHVV$ interactions. This is in contrast to the SM case, where the two interaction vertices are correlated by $vV_{HHVV} = V_{HVV}$, with $v = 246$ GeV, and this relation appears as a consequence of H being a component of the SM doublet. Going BSM, other different correlations between a and b and, therefore, between the HVV and $HHVV$ interactions at low energies, are expected to appear. For instance, considering small deviations from the SM values, $\Delta a \equiv 1 - a$ and $\Delta b \equiv 1 - b$, in the case of BSM theories that incorporate the Higgs boson as a component of a $SU(2)$ doublet, correlations between a and b appear. This is the case of the SMEFT, where these correlations among a and b translate into a correlation between Δa and Δb given specifically by $4\Delta a = \Delta b$ (see, for instance, [12, 13]). In contrast, for a two-Higgs-doublet model (2HDM), once the heavy Higgs modes H^\pm , H^0 and A are integrated out, a different correlation between a and b leading to $2\Delta a = -\Delta b$ appears (see [14]). Thus, there is a clear motivation to explore whether such correlations can be checked experimentally at future colliders.

The aim of the present work is to discuss the phenomenological implications of BSM HVV and $HHVV$ couplings within the HEFT, specifically in the double Higgs production with two light jets at the LHC, i.e. in $pp \rightarrow HHjj$. Since our main purpose here is to explore the expected sensitivity at the LHC to the previously mentioned correlations via the particular combination $(\kappa_V^2 - \kappa_{2V})$, we will focus our study on the $HHjj$ events with vector boson fusion (VBF) topology. This $HHjj$ production with VBF topology is known to be the second-largest HH production mode at LHC, behind gluon-gluon fusion, and has the advantage of allowing us access to the two κ_V and κ_{2V} parameters together in just one process. The

relevant remark for the present work is that this dependence on κ_V and κ_{2V} appears in $HHjj$ via VBF precisely through this particular combination $(\kappa_V^2 - \kappa_{2V})$. This can be easily understood from the large energy behaviour of the dominant helicity scattering amplitude for the subprocess of HH production from the fusion of two EW gauge bosons, $VV \rightarrow HH$ with $VV = WW, ZZ$. This dominant subprocess is known to be that of the longitudinal modes, i.e., $V_L V_L \rightarrow HH$. Specifically, at large energies compared to the boson masses, $\sqrt{s} \gg m_H, m_V$, this amplitude $\mathcal{A}(V_L V_L \rightarrow HH)$ within the HEFT behaves as $\simeq -(a^2 - b)s/v^2$, with v the EW vacuum expectation value (see, for instance, [13], [15]). And it is this dependence what is approximately transmitted to the full process, $pp \rightarrow HHjj$. Furthermore, it has been shown in [15] that also the differential cross section with respect to the final Higgs pseudo-rapidity η_H manifests the relevance of this particular combination. Specifically, $d\sigma(VV \rightarrow HH)/d\eta_H$ shows clearly a central peak at $\eta_H = 0$ when $(\kappa_V^2 - \kappa_{2V}) \neq 0$ and, in addition, the height of this peak is correlated with the size of the $(\kappa_V^2 - \kappa_{2V})$ combination, indicating that the final Higgs bosons in $VV \rightarrow HH$ within the HEFT are produced with high transversality as compared to the SM case.

The final objective of this work is to explore the sensitivity at LHC to this $(\kappa_V^2 - \kappa_{2V})$ combination, both in the total cross section and also in specific differential cross-section distributions with respect to variables that properly show the best sensitivity to this particular combination. There exist some previous studies focusing on the role of this specific combination. For e^+e^- colliders we refer to [15, 16], and for pp colliders an important work making reference to this issue was done some time ago in [17]. In this work, we will focus on the access to $(\kappa_V^2 - \kappa_{2V})$ in pp collisions considering the particular final state $b\bar{b}\gamma\gamma jj$, having two b -jets, two photons and two light jets. Thus, the full process for the present study of BSM signals is $pp \rightarrow HHjj \rightarrow b\bar{b}\gamma\gamma jj$, where the final Higgs bosons decay to $H \rightarrow b\bar{b}$ and $H \rightarrow \gamma\gamma$, respectively. For this purpose, we will first show the HEFT predictions at the parton-level for $pp \rightarrow HHjj$, for both the total cross section and the most relevant differential cross sections, and then we will move to a more realistic computation for the full process $pp \rightarrow b\bar{b}\gamma\gamma jj$ including showering, hadronization, clustering, and detector level effects. The events simulations in this work are produced with MG5 (aMC@NLO version-3.5.1 Montecarlo event generator [18]), where we have implemented our HEFT model defined in Refs. [9–12], and all the final events will be filtered with PYTHIA [19] and DELPHES [20] to incorporate the showering, hadronization, clustering, and detector level effects. Specifically, for the detector, we choose CMS. The Phase-2 upgraded CMS detector will be simulated using DELPHES for a fast and parametric detector simulation [21]. For the predictions at the future HL-LHC, we use $\sqrt{s} = 14$ TeV and the high luminosity option with integrated luminosity of 3000 fb^{-1} . For the partons involved in the proton-proton collisions, we use the set of parton distribution functions (PDFs) NNPDF2.3 [22]. The final part of the work is devoted to showing the improvement one can get on the sensitivity to this $(\kappa_V^2 - \kappa_{2V})$ combination at HL-LHC by means of the proper selection of variables and cuts on the final state, that are good discriminants between the signal and main background. In this last study, we will also propose several strategies focusing on the variables of the final $\gamma\gamma$ and b -jets pairs.

The outline of the present work is as follows. Section 2 present a short review of the HVV and $HHVV$ effective interactions within HEFT and their relation to the κ formalism. In section 3 we recall the role of $(\kappa_V^2 - \kappa_{2V})$ in Higgs pair production from VBF. In section 4 we present the details of our analysis of $HHjj$ production within the HEFT at proton-proton collisions, including our selection strategies for both the total $HHjj$ event rates and the relevant distributions. Section 5 is devoted to the analysis and the prospects for the full process $pp \rightarrow HHjj' \rightarrow b\bar{b}\gamma\gamma jj'$ at LHC, including all the realistic effects from showering, hadronization, clustering, and detector in both the total cross section and the most relevant differential cross sections. Section 6 presents our final results and strategies for the improvement of the sensitivity to $(\kappa_V^2 - \kappa_{2V})$ in the future HL-LHC. The last section summarizes our conclusions.

2 HVV and $HHVV$ interactions within HEFT: relation to the κ -formalism

In this section, we review the main aspects of BSM Higgs physics within HEFT, and its relation to the κ -formalism.

The HEFT, also called EChL (Electroweak Chiral Lagrangian) in the literature, is built from a gauge principle based on the requirement of EW gauge invariance $SU(2)_L \times U(1)_Y$. It has an additional global symmetry, called EW chiral symmetry, $SU(2)_L \times SU(2)_R$ (resembling the chiral symmetry of low energy QCD), which is spontaneously broken to the diagonal subgroup $SU(2)_{L+R}$ also called the custodial symmetry group.

In analogy to QCD's χ PT and by means of a unitary matrix U , the GBs of the EW theory are embedded using an exponential representation. The U matrix transforms linearly as a bi-doublet under chiral rotations $SU(2)_L \times SU(2)_R$, $U' = LUR^\dagger$, whereas the GBs transform non-linearly, being this later a feature which is characteristic of chiral Lagrangians. The GBs fields in the EW case are normalized by the EWSB scale, $v = 256$ GeV, in contrast to χ PT, where the GBs are normalized by the pion decay constant $f_\pi = 94$ MeV. The introduction of the SM gauge bosons in the HEFT is usually performed by means of the covariant derivative. All these features and pieces of the HEFT and the EChL are summarized in the following.

The relevant effective bosonic operators for the present work are contained in the Leading Order (LO) HEFT Lagrangian with chiral dimension 2. Therefore, here we restrict ourselves to this bosonic LO-HEFT Lagrangian. In the following, we recall this LO-HEFT Lagrangian for arbitrary covariant R_ξ gauges which was introduced in a series of works [9–12]. We use here the same notation as in those works:

$$\begin{aligned} \mathcal{L}_{\text{LO}}^{\text{HEFT}} = & \frac{v^2}{4} \left(1 + 2a \frac{H}{v} + b \frac{H^2}{v^2} + \dots \right) \text{Tr}[D_\mu U^\dagger D^\mu U] + \frac{1}{2} \partial_\mu H \partial^\mu H - V(H) \\ & - \frac{1}{2g^2} \text{Tr}[\hat{W}_{\mu\nu} \hat{W}^{\mu\nu}] - \frac{1}{2g'^2} \text{Tr}[\hat{B}_{\mu\nu} \hat{B}^{\mu\nu}] + \mathcal{L}_{GF} + \mathcal{L}_{FP}. \end{aligned} \quad (2.1)$$

The relevant fields and quantities appearing in this Lagrangian are the following. H is the Higgs boson field, which is introduced in the HEFT as a singlet field, in contrast to the SM or the SMEFT, where it is introduced inside a component of the usual doublet Φ . The U field is a 2×2 matrix which in the exponential representation is given by:

$$U = \exp\left(i \frac{\omega_i \tau_i}{v}\right), \quad (2.2)$$

that contains the three GB fields ω_i ($i = 1, 2, 3$) in a non-linear representation of the $SU(2)$ symmetry group, and τ_i are the three Pauli matrices. The EW covariant derivative of this U field is given by:

$$D_\mu U = \partial_\mu U - i \hat{W}_\mu U + i U \hat{B}_\mu, \quad (2.3)$$

that contains the EW gauge fields, $\hat{W}_\mu = \frac{g}{2} W_\mu^i \tau^i$ and $\hat{B}_\mu = \frac{g'}{2} B_\mu \tau^3$ and the EW gauge couplings g and g' . The corresponding EW field strength tensors are given respectively by:

$$\hat{W}_{\mu\nu} = \partial_\mu \hat{W}_\nu - \partial_\nu \hat{W}_\mu - i[\hat{W}_\mu, \hat{W}_\nu], \quad \hat{B}_{\mu\nu} = \partial_\mu \hat{B}_\nu - \partial_\nu \hat{B}_\mu. \quad (2.4)$$

\mathcal{L}_{GF} and \mathcal{L}_{FP} are the proper gauge fixing and Fadeev-Popov terms for the R_ξ covariant gauges (for details, see the previously quoted references). Notice that we use here the same sign conventions as in Ref.[13], such that the FRs for $a = b = \kappa_3 = \kappa_4 = 1$ coincide (also in sign) with the SM FRs set in MG5.

$i\Gamma_{HW_\mu W_\nu}^{\text{SM}} = igm_W g_{\mu\nu}$	$i\Gamma_{HZ_\mu Z_\nu}^{\text{SM}} = i\frac{g}{\cos\theta_W} m_Z g_{\mu\nu}$	$i\Gamma_{HHW_\mu W_\nu}^{\text{SM}} = i\frac{g^2}{2} g_{\mu\nu}$	$i\Gamma_{HHZ_\mu Z_\nu}^{\text{SM}} = i\frac{g^2}{2\cos^2\theta_W} g_{\mu\nu}$
$i\Gamma_{HW_\mu W_\nu}^{\text{HEFT}} = ia gm_W g_{\mu\nu}$	$i\Gamma_{HZ_\mu Z_\nu}^{\text{HEFT}} = ia\frac{g}{\cos\theta_W} m_Z g_{\mu\nu}$	$i\Gamma_{HHW_\mu W_\nu}^{\text{HEFT}} = ib\frac{g^2}{2} g_{\mu\nu}$	$i\Gamma_{HHZ_\mu Z_\nu}^{\text{HEFT}} = ib\frac{g^2}{2\cos^2\theta_W} g_{\mu\nu}$

Table 2.1. Higgs-EW gauge boson interaction's Feynman rules within SM and HEFT frameworks. Here, $g_{\mu\nu}$ denotes the metric tensor. The HEFT coefficients a (in red) and b (in blue) can be replaced by κ_V and κ_{2V} respectively.

The physical gauge fields are then given by:

$$W_\mu^\pm = \frac{1}{\sqrt{2}}(W_\mu^1 \mp iW_\mu^2), \quad Z_\mu = c_W W_\mu^3 - s_W B_\mu, \quad A_\mu = s_W W_\mu^3 + c_W B_\mu, \quad (2.5)$$

where we have used the short notation $s_W = \sin\theta_W$ and $c_W = \cos\theta_W$, with θ_W the weak angle.

$V(H)$ is the Higgs potential within the HEFT, which includes the modified triple and quartic Higgs self-interactions:

$$V(H) = \frac{1}{2}m_H^2 H^2 + \kappa_3 \lambda v H^3 + \kappa_4 \frac{\lambda}{4} H^4. \quad (2.6)$$

Notice that the relations among the physical boson masses and couplings within the LO-HEFT are as in the SM. Concretely, $m_W = gv/2$, $m_Z = m_W/\cos\theta_W$ and $m_H^2 = 2\lambda v^2$, where $v = (\sqrt{2}G_F)^{-1/2} = 246$ GeV. Notice also that because H is a singlet within the HEFT, the Higgs interactions with the gauge bosons are encoded by generic polynomials $\mathcal{F}_i(H)$ with completely arbitrary coefficients. In particular, the Higgs interactions with the EW gauge bosons are encoded in $\mathcal{F}(H)$, which includes the parameters a and b of our interest in this work:

$$\mathcal{F}(H) = \left[1 + 2a\frac{H}{v} + b\frac{H^2}{v^2} \dots \right]. \quad (2.7)$$

For the explicit computations in the following sections, we will simplify the HEFT model assuming $\kappa_3 = \kappa_4 = 1$ and leave only the two relevant LO-HEFT parameters, a and b , describing the new Higgs effective couplings. The interaction vertices we are interested in, HVV and $HHVV$, are present in the first term of Eq. 2.1, which incorporates the covariant derivatives of the matrix U . From the expansion of U , Feynman rules (FRs) for the HVV and $HHVV$ ($V = W, Z$) and other vertices within the HEFT are obtained in general gauges. In particular, to get them in the unitary gauge one takes $U = 1$ and rotates the bosonic fields to the physical basis. These rules are similar to those from the SM, except for the a and b effective coefficients, which in the SM are equal to 1. In this present work, there is no need to consider higher-order terms of $\mathcal{F}(H)$. We summarize in Table 2.1 the set of relevant HEFT Feynman Rules (FR). We have also included the SM Feynman rules for comparison. It is worth noting that all HEFT FR preserve the original SM tensor structure, and this is the reason why the HEFT a and b coefficients can be directly identified with the κ_V and κ_{2V} modifiers, respectively.

The present data from LHC set important constraints on these κ parameters, which can be translated directly into constraints on the LO-HEFT parameters $a = \kappa_V$, $b = \kappa_{2V}$ and $\kappa_3 = \kappa_\lambda$. The constraints on κ_4 are very weak yet. For the present work, we select the following set of constraints to the values of the Higgs-gauge couplings and Higgs self-coupling:

$$\text{ATLAS (95\%CL)} : \kappa_V \in [0.99, 1.11], \quad \kappa_{2V} \in [0.6, 1.5], \quad \kappa_\lambda \in [-1.2, 7.2], \quad (2.8)$$

taken from [23] and [24], and

$$\text{CMS (95\%CL)} : \kappa_V \in [0.97, 1.09], \quad \kappa_{2V} \in [0.6, 1.4], \quad \kappa_\lambda \in [-1.2, 7.5], \quad (2.9)$$

taken from [25] and [26].

In a recent paper, [6], a summary by ATLAS and CMS collaborations is presented, with references to some improved constraints and the prospective improvements for the future operation of HL-LHC. For the main focus of the present paper, it is important to remark that no direct constraints have been set so far on the combination parameter of our interest here, $(\kappa_V^2 - \kappa_{2V})$.

3 The role of $(\kappa_V^2 - \kappa_{2V})$ in Higgs pair production from VBF

In this section, we explain shortly why the specific combination of κ modifiers given by $\kappa_V^2 - \kappa_{2V}$ plays an important role in Higgs pair production at colliders. For this, we first tell on the main aspects of the scattering amplitude of the subprocess $VV \rightarrow HH$, which is involved at colliders within the LO-HEFT framework introduced before, and then discuss their implications on the cross-section and differential cross-sections. We consider here the two interesting cases, with VV being either WW or ZZ . The most relevant subprocess for the pp collisions, explored in the next section, is known to be $WW \rightarrow HH$, both for the SM and HEFT cases. The double Higgs production rates coming from ZZ fusion at the LHC are known to be much smaller than those from WW fusion, due to the reduced luminosity for radiating ZZ pairs from the pp compared to radiating WW pairs. However, to be complete in the forthcoming estimates for the LHC in the next section, all the channels will be taken into account here.

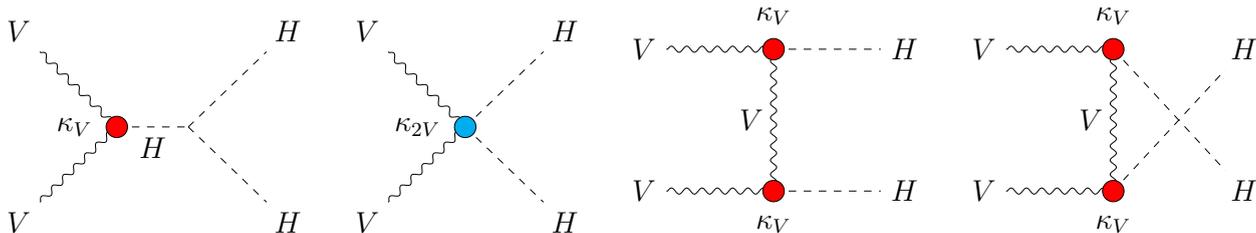


Figure 3.1. Feynman diagrams contributing to $VV \rightarrow HH$ (with $VV = WW, ZZ$) within the HEFT in the Unitary gauge. From left to right, diagrams for the s-channel, contact c-channel, t-channel and u-channel. Effective vertices proportional to $\kappa_V = a$ and $\kappa_{2V} = b$ are colored in red and blue, respectively.

As we said before, the considered BSM theory only involves modifications of the interaction vertices between the scalar and massive gauge bosons. At pp colliders, we expect the leading contribution to the partonic $q_1 q_2 \rightarrow q_3 q_4 HH$ BSM signal to come from the vector boson $VV \rightarrow HH$ ($V = W^\pm, Z$) scattering subprocess. Other channels not mediated by VBF are known to be subdominant (see, for instance, Ref. [27]). Compared to the production of a Higgs boson pair through a lepton initial state, hadron collisions involve a wider variety of possible initial partons (we refer the reader to appendix A for the complete list of topologies). Both neutral and charged vector bosons have to be taken into consideration when determining the double Higgs production amplitude through VBF.

All diagrams contributing to the tree-level amplitude of the VBF subprocess in the unitary gauge are included in Figure 3.1. Amplitudes, contrary to observables such as the cross-section, provide us with information on all kinematics of an event. Since the amplitude is not expected to be modified by a certain gauge choice, due to gauge invariance, we choose here the simplest unitary gauge, reached by setting $U = 1$ in the HEFT Lagrangian, which avoids involving any diagram with GB internal lines. With this particular section, we aim to illustrate the sensitivity of this subprocess to the particular combination of our interest $a^2 - b$, or equivalently $\kappa_V^2 - \kappa_{2V}$, in terms of κ modifiers.

The individual contribution of each diagram to the scattering amplitude of $V(p_1)V(p_2) \rightarrow H(p_3)H(p_4)$, corresponding to s -channel, contact c -channel, t -channel, and u -channel, respectively, can be written as:

$$\mathcal{A}_s = a \frac{3g^2\delta}{2m_W} \frac{m_H^2}{s - m_H^2} (\epsilon_1 \cdot \epsilon_2) \quad (3.1) \quad \mathcal{A}_t = a^2 g^2 \frac{\delta^2}{t - m_V^2} \left((\epsilon_1 \cdot \epsilon_2) + \frac{(\epsilon_1 \cdot p_3)(\epsilon_2 \cdot p_4)}{m_V^2} \right) \quad (3.3)$$

$$\mathcal{A}_c = b \frac{g^2\beta}{2} (\epsilon_1 \cdot \epsilon_2) \quad (3.2) \quad \mathcal{A}_u = a^2 g^2 \frac{\delta^2}{u - m_V^2} \left((\epsilon_1 \cdot \epsilon_2) + \frac{(\epsilon_1 \cdot p_4)(\epsilon_2 \cdot p_3)}{m_V^2} \right) \quad (3.4)$$

$$\text{where } \delta = \begin{cases} m_W & V = W^\pm \\ \frac{m_Z}{\cos\theta_W} & V = Z \end{cases} \text{ and } \beta = \begin{cases} 1 & V = W^\pm \\ -\frac{1}{\cos^2\theta_W} & V = Z \end{cases}$$

Since the FR have the same tensor dependence independently of the considered vector boson W^\pm, Z , with their only difference being present in the coupling constants and the masses, a general term for each diagram's amplitude can be obtained. δ and β parameters are introduced to particularize results either to W^\pm or Z mediated processes $\epsilon_{1,2}$ identify the massive boson's polarization modes, and $p_{3,4}$ identify the Higgs' 4-momenta.

The parameter κ_{2V} is exclusively accessible through the contact diagram, justifying requiring Higgs boson pair production processes by VBF to be accessible. Effectively, κ_{2V} contributes directly to the scattering amplitude, marking a qualitative and quantitative physical difference from κ_V . The rest of the diagrams involve κ_V , with order 1 in the s -channel diagram and order 2 in the t -channel and u -channel diagrams. The contribution of κ_V to the amplitude is expected to be of order κ_V^2 . These last statements are directly related to the behavior of the amplitude at high energies, as it has already been shown in [15]. At high energies, the dominant helicity amplitude is the one for the longitudinal modes, which at high energies grows with the VBF subprocess energy. This can be understood by means of the Equivalence Theorem (ET) [28–30] that states the equality of scattering amplitudes at high energies if one replaces the external longitudinal gauge bosons by the corresponding GBs. In the present case, the ET implies in particular: $\mathcal{A}(W_L^+ W_L^- \rightarrow HH) \simeq \mathcal{A}(\omega^+ \omega^- \rightarrow HH)$ for $\sqrt{s} \gg m_W$. This can be explicitly shown by comparing our next results (Equation 3.7) with the results, for instance, in [31], where they use the ET. On the other hand, a complete analysis going beyond the leading order considered here of the scattering amplitude for the full $WW \rightarrow HH$ process, including all the relevant HEFT operators up to next to leading order, and with the explicit comparison of the different polarization channels can be found in [12].

Next, we shortly review the computations of the LO-HEFT amplitude for the longitudinal gauge bosons, $\mathcal{A}^L = \mathcal{A}(V_L V_L \rightarrow HH)$. Here we are interested in the high energy limit, i.e., for $\sqrt{s} \gg m_V, m_H$. For this exercise, we use the Center of Mass (CM) frame, and write the momenta of the Higgs bosons and polarization vectors for the longitudinal modes in terms of the CM energy \sqrt{s} , the particle masses, and the CM scattering angle θ :

$$p_{3,4} = \left(\frac{\sqrt{s}}{2}, \pm \sin\theta \frac{\sqrt{s - 4m_H^2}}{2}, 0, \pm \cos\theta \frac{\sqrt{s - 4m_H^2}}{2} \right), \quad (3.5)$$

$$\epsilon_{1,2}^L = \left(\frac{\sqrt{s - 4m_V^2}}{2m_V}, 0, 0, \frac{\pm\sqrt{s}}{2m_V} \right).$$

Then, considering the high energy limit, $\sqrt{s} \gg m_V, m_H$, in the previous amplitudes, taking $\epsilon_{1,2} = \epsilon_{1,2}^L$, and using the following high energy limit for the Mandelstam variables:

$$t \simeq -\frac{s}{2} (1 - \cos\theta), \quad u \simeq -\frac{s}{2} (1 + \cos\theta)$$

we get the leading terms of the amplitude with respect to the s variable, which we separate into the various contributions from the various diagrams:

$$\mathcal{A}^L = \mathcal{A}_s^L + \mathcal{A}_c^L + \mathcal{A}_t^L + \mathcal{A}_u^L \quad (3.6)$$

where:

$$\begin{aligned} \mathcal{A}_s^L &= \mathcal{O}(s^0) & \mathcal{A}_t^L &= -a^2 g^2 \frac{\delta^2}{8m_V^4} (1 - \cos\theta) s + \mathcal{O}(s^0) \\ \mathcal{A}_c^L &= b \frac{g^2 \beta}{4m_V^2} s + \mathcal{O}(s^0) & \mathcal{A}_u^L &= -a^2 g^2 \frac{\delta^2}{8m_V^4} (1 + \cos\theta) s + \mathcal{O}(s^0) \end{aligned}$$

The total amplitude at high energies, $\sqrt{s} \gg m_H, m_V$, is then the following:

$$\mathcal{A}^L = -(a^2 - b) \frac{g^2 \beta}{8m_V^2} s + \mathcal{O}(s^0) \quad (3.7)$$

where we see explicitly the announced combination of HEFT coefficients ($a^2 - b$). Therefore, the high energy behavior of the VBF scattering amplitude for longitudinal gauge bosons exhibits the linear dependence on the κ framework combination ($\kappa_V^2 - \kappa_{2V}$). In the particular case of the SM, i.e. , for $\kappa_V, \kappa_{2V} = 1$, the linear term of order s vanishes and the resulting SM amplitude is of $\mathcal{O}(s^0)$. Following from the expression of \mathcal{A}^L , this vanishing is not exclusive to the SM, thus expecting similar high energy behaviour for the set of HEFT models whose κ parameters are such that $(\kappa_V^2 - \kappa_V) = 0$, or equivalently for BSM physics where the κ 's are related by $\kappa_V^2 = \kappa_{2V}$. This particular behaviour will help us in identifying the most interesting BSM scenarios where this relation is not fulfilled, therefore their experimental signals will be better distinguishable from the SM ones. Our main objective here is precisely to focus on these particular BSM scenarios with $(\kappa_V^2 - \kappa_V) \neq 0$, and explore which kind of experimental measurements and types of observables could be more sensitive to this particular combination.

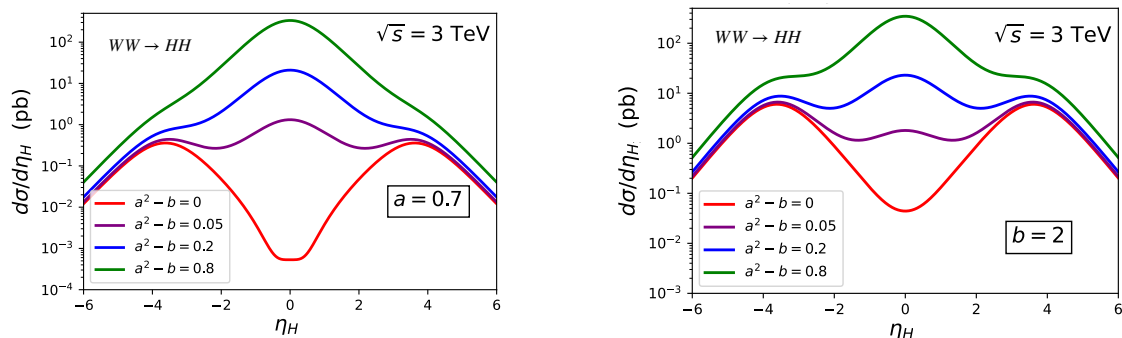


Figure 3.2. Predictions within the HEFT for the differential cross section of $WW \rightarrow HH$ with respect to the final Higgs rapidity, η_H . The colored lines are for different choices of the combination $(a^2 - b)$ defining some examples of BSM scenarios. We take $(a^2 - b) = 0$ (red line), 0.05 (purple line), 0.2 (blue line) and 0.8 (green line). Here the total center-of-mass energy is fixed to $\sqrt{s} = 3$ TeV. The plot on the left is for $a = 0.7$, and the plot on the right is for $b = 2$.

As in Ref. [15], we focus here on the search for particular differential cross-sections to be measured at future colliders which are especially sensitive to the value of $(\kappa_V^2 - \kappa_V) \neq 0$. Given the above shown behaviour of the amplitudes with the scattering angle θ , it is obvious that the most sensitive differential cross sections to this combination are those with respect to the angular variables of the final Higgs bosons or their decay products. Concretely, some examples are: $d\sigma/d(\cos\theta)$, $d\sigma/d\eta_H$, and $d\sigma/dp_H^T$, where σ refers to the unpolarized cross section, and η_H and p_H^T are the Higgs pseudo-rapidity and Higgs transverse momentum, respectively. For instance, in the case of η_H this sensitivity to $(a^2 - b)$ can be seen

in Fig.3.2. Other examples can be found in Ref. [15]. We see that the higher the value of $(a^2 - b)$ is, the more transversely the Higgs boson is produced, since the central peak at $\eta_H = 0$ is more pronounced. We wish to emphasize, that this behaviour of the final H showing a high transversality is genuine of HEFT models with $(\kappa_V^2 - \kappa_V) \neq 0$ and the height of the central peak is correlated with this combination value, and it is not much dependent on the separate values of κ_V and κ_{2V} . This can be seen clearly comparing the two plots in Fig. 3.2 that assume different values for the two involved κ 's, or equivalently, different values for a and b , and both manifest the highest central peak at the highest value of $a^2 - b$, here fixed to 0.8.

Therefore, from a collider perspective, these HEFT models will provide BSM signals where the Higgs bosons (or their decay products) are produced highly transverse, i.e. , with angular distances closer to the plane transverse to the beam axis. We refer the reader to Ref. [15], where more examples are included and a more detailed analysis of the subprocess differential cross-sections is performed. The consequences of the previously commented sensitivity of the described subprocess to the combination $(a^2 - b)$ will be translated to the context of the real scattering process. This was explored in Ref. [15] for the case of e^+e^- colliders. In the present work, we will explore this sensitivity in the case of hadronic pp colliders. Finding the proper differential cross section distributions showing this sensitivity for the full process $pp \rightarrow HHjj$ is indeed one of our main objectives in this work. This issue will be studied in the following sections.

4 Exploring $HHjj$ production in pp collisions within HEFT

In this section, the HEFT predictions for $HHjj$ production from pp collisions are presented and analyzed. First we evaluate the integrated cross-section for $pp \rightarrow HHjj'$ with VBF topology as a function of a , b , and the combination $a^2 - b$. Then, we introduce the main phenomenology of Higgs boson pair angular kinematics resulting from BSM within the HEFT framework, and study the most interesting effects on the proper distributions with these angular variables as a function of this same $a^2 - b$ combination. Throughout this section, only the parton-level signals produced using MG5 [18] simulations have been considered.

4.1 Vector Boson Fusion (VBF): Events selection strategy

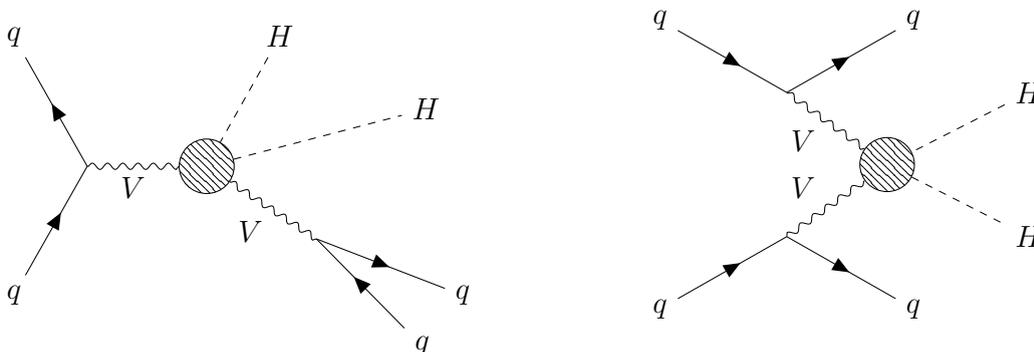


Figure 4.1. Schematic of the two different topology classes involved in the EW Higgs boson pair production in pp collisions, the associated production (double Higgs-strahlung) [left] and the vector boson fusion (VBF) [right]. Here, V refers generically to either W^\pm or Z and q denotes either quarks q or anti-quarks \bar{q} .

Our first step here is the selection of $HHjj$ events with VBF topology from the complete set of possible topologies in the partonic $q_1q_2 \rightarrow HHq_3q_4$ process, which are schematically represented in figure 4.1. Notice that the initial and final quarks q refer generically to either quarks or anti-quarks. The full set of Feynman diagrams for the case $q_1\bar{q}_2 \rightarrow HHq_3\bar{q}_4$ is displayed in appendix A. Recall also that the particular diagrams including the subprocess $VV \rightarrow HH$ cannot be just extracted by hand, since excluding the other diagrams from the sample simulation would break gauge invariance. However, it is well known that events with VBF topology can be efficiently selected, preserving gauge invariance by the proper cuts on the two final light jets jj' , which are typically emitted in narrow cones and in opposite hemispheres, being easily differentiated from non-VBF jet pairs. Both light jets in the final state acquire a moderate absolute pseudo-rapidity, typically in the range $2 \leq |\eta_j| \leq 5$, and a notable pseudo-rapidity difference between themselves. This is true not only for the SM case but also for all BSM cases within the HEFT [27, 32–36].

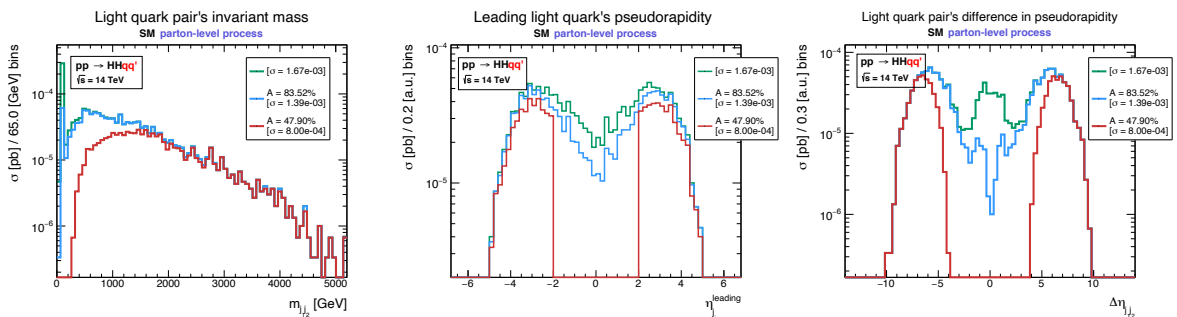


Figure 4.2. Parton-level SM differential cross section of the double Higgs production with respect to the light quark pair’s invariant mass [left], the light quark’s pseudo-rapidity [center] and to the light quarks pseudo-rapidity difference [right], for different kinematic cuts applied to the event’s phase space. In green, the initial signal. In blue, reduced to events with $\eta_{j_1} \times \eta_{j_2} < 0$, with an acceptance of 83.52 %. In red, reduced to events with $\eta_{j_1} \times \eta_{j_2} < 0$, as well as $|\eta_j| > 2$, with an acceptance of 47.90 %.

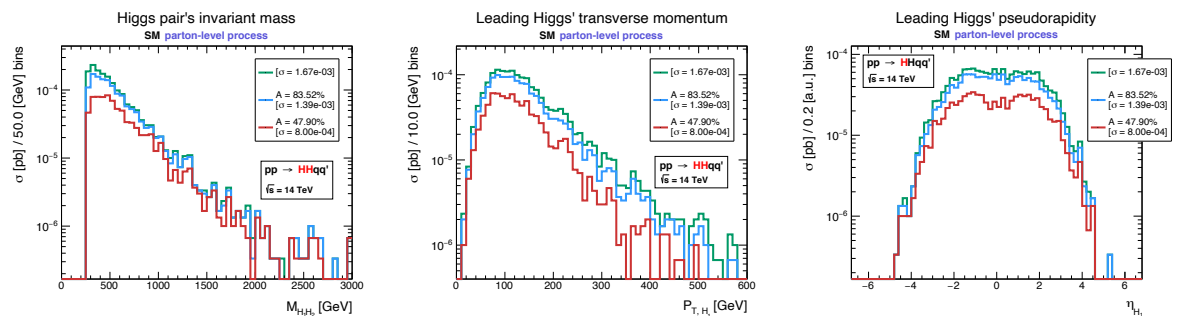


Figure 4.3. Parton-level SM differential cross section of the double Higgs production with respect to the Higgs boson pair’s invariant mass [left], the leading Higgs transverse momentum [center] and to the leading Higgs pseudo-rapidity [right], for different kinematic cuts applied to the event’s phase space. In green, the initial signal. In blue, reduced to events with $\eta_{j_1} \times \eta_{j_2} < 0$, with an acceptance of 83.52 %. In red, reduced to events with $\eta_{j_1} \times \eta_{j_2} < 0$, as well as $|\eta_j| > 2$, with an acceptance of 47.90 %.

Figures 4.2 and 4.3 show the predictions for the SM differential cross-section of the $pp \rightarrow HHjj'$ process at the partonic level with respect to several kinematic variables. Figure 4.2 includes, from left to right, the differential cross-section with respect to the invariant mass of the jet pair, the leading

S_0	$P_{T,j} > 20.0 \text{ GeV}$	$ \eta_j < 5.0$	$\Delta R_{j,j} > 0.4$		
S_1	$P_{T,j} > 20.0 \text{ GeV}$	$ \eta_j < 5.0$	$\Delta R_{j,j} > 0.4$	$\eta_{j_1} \times \eta_{j_2} < 0$	
S_2	$P_{T,j} > 20.0 \text{ GeV}$	$ \eta_j < 5.0$	$\Delta R_{j,j} > 0.4$	$\eta_{j_1} \times \eta_{j_2} < 0$	$ \eta_j > 2$

Table 4.1. Summary of the kinematic cuts applied to SM signals in Figures 4.2 and 4.3.

jet’s pseudo-rapidity, and the jets’ pseudo-rapidity difference. Figure 4.3 shows, from left to right, the differential cross-section with respect to the Higgs boson pair’s invariant mass, the leading, in P_T , Higgs boson’s P_T , and the leading Higgs boson’s pseudo-rapidity. All signals are generated with the following set of basic cuts:

$$P_{T,j} > 20.0 \text{ GeV}, \quad |\eta_j| < 5.0, \quad \Delta R_{j,j} > 0.4 \quad (4.1)$$

Green distributions only involve said basic cuts. The invariant mass distribution in green from Figure 4.2 shows two maxima, approximately at $m_{jj'} \approx 500 \text{ GeV}$ and $m_{jj'} \approx 0$. The latter is directly related to resonant diagrams, and we expect this maximum to be present at either $m_W = 80$ or $m_Z = 91 \text{ GeV}$. In the pseudo-rapidity difference distribution three maxima can be found, one around $|\Delta\eta_{jj}| \approx 0$ and the other two at $|\Delta\eta_{jj}| \approx 6$. The first maximum is related to topologies that generate two collimated jets. Said kinematics regions, i.e. $m_{jj'} \approx 0$ and $|\Delta\eta_{jj}| \approx 0$, do not correspond to VBF events.

In order to isolate the VBF events, we will first check the results of applying two kinematic cuts to the pseudo-rapidity of the jets:

$$\eta_{j_1} \times \eta_{j_2} < 0, \quad |\eta_j| > 2 \quad (4.2)$$

Blue distributions present in Figures 4.2 and 4.3 correspond to the parton-level signal filtered for events whose jets pseudo-rapidity have opposite signs $\eta_{j_1} \times \eta_{j_2} < 0$, that is, evolve in opposed directions with respect to the beam’s axis. For the case of the jet pair invariant mass distribution, the blue signal shows a reduction of almost one order of magnitude in the number of resonant events. In the central region of the jet pseudo-rapidity difference distribution, the maximum is now a minimum. Red distributions correspond to the parton-level signal filtered for both criteria present in equation 4.2. The differential cross-section with respect to the jet pseudo-rapidity difference perfectly fits a $4 < |\Delta\eta_{jj}| < 10$ distribution, resulting from the final individual $2 < |\eta_j| < 5$ selection cut. The jet pair invariant mass distributions do not include a visible resonant contribution, and the non-resonant maximum has moved closer to $m_{jj'} \approx 1000 \text{ GeV}$.

From Figure 4.3, we conclude that all differential cross-section distributions with respect to the Higgs boson’s kinematics, for either the initial or the filtered signal, have the same exact profile. The only visible difference is in the scale, related to the number of events resulting from each selection process. The kinematics of the generated Higgs boson pair are not affected by applying both kinematic cuts.

The acceptance for the SM case results of imposing both kinematic cuts, defined as the quotient of the filtered events over the total number of events, $A = \frac{N_{cut}}{N_{orig}}$, is $A = 47.90\%$. Thus, for this SM scenario, the events with VBF topology contribute to 50% of the total number of events. Extending this type of analysis to all BSM scenarios within the HEFT framework considered in this work, we find an acceptance for this event selection with VBF topology ranging between 50% and 75% in agreement with [27].

In summary, the final selection strategy applied to all parton-level signals generated using MG5 in order to isolate the events with VBF topology, for both the SM and HEFT predictions of the $pp \rightarrow HHjj'$ process, is composed of the following 5 kinematic cuts:

Event selection			
VBF topology	$P_{T,j} > 20.0$ GeV	$2 < \eta_j < 5$	$\eta_j \times \eta_{j'} < 0$
	$m_{jj'} > 500$ GeV	$\Delta R_{jj} > 0.4$	

Table 4.2. Event selection strategy for VBF topologies, used for theoretical predictions for the $pp \rightarrow HHjj'$ process.

The selection strategy described in Table 4.2 will be referred to as the VBF selection strategy. The strategy involves all kinematics cuts discussed throughout this subsection, either basic and jet pseudo-rapidity cuts, as well as cuts to the invariant mass of the light jet pair, $m_{jj'} > 500$ GeV, to further isolate the VBF configuration. Indeed, this selection strategy will also be presented for the recalculated prediction, including the $b\bar{b}\gamma\gamma jj'$ final state.

4.2 HEFT total cross section, $\sigma(pp \rightarrow HHjj')$, versus $(\kappa_V^2 - \kappa_{2V})$

In this section, we present the predictions of the total cross section for the hadronic process, $\sigma(pp \rightarrow HHjj')$, within the context of the HEFT, and analyze the results as a function of the combination of the κ parameters of our interest, given by $(\kappa_V^2 - \kappa_{2V})$. We first analyze the sensitivity to the HEFT parameters a and b separately, and then show the relevance of combining them particularly into $(a^2 - b)$. We expect the sensitivity to particular HEFT models of the process $pp \rightarrow HHjj'$ to inherit most of the properties we discussed in section 3 for the $VV \rightarrow HH$ subprocess.

For this analysis, we simplify the constituents of the protons to include just the two lightest generations and the gluons, $p \equiv gu\bar{u}d\bar{d}s\bar{s}c\bar{c}$. For the process of our interest, $pp \rightarrow HHjj'$, the relevant partonic subprocess, $q_1q_2 \rightarrow HHq_3q_4$, is folded with the proper Parton Distribution Function (PDF's) for the quarks and antiquarks inside the proton, chosen to be NNPDF2.3 [22]. The simulations make use of a diagonal Cabibbo-Kobayashi-Maskawa (CKM) matrix, which is a very good approximation for the present computation. For this subsection and the following, Subsection 4.3, the VBF selection strategy detailed in Table 4.2 has been applied.

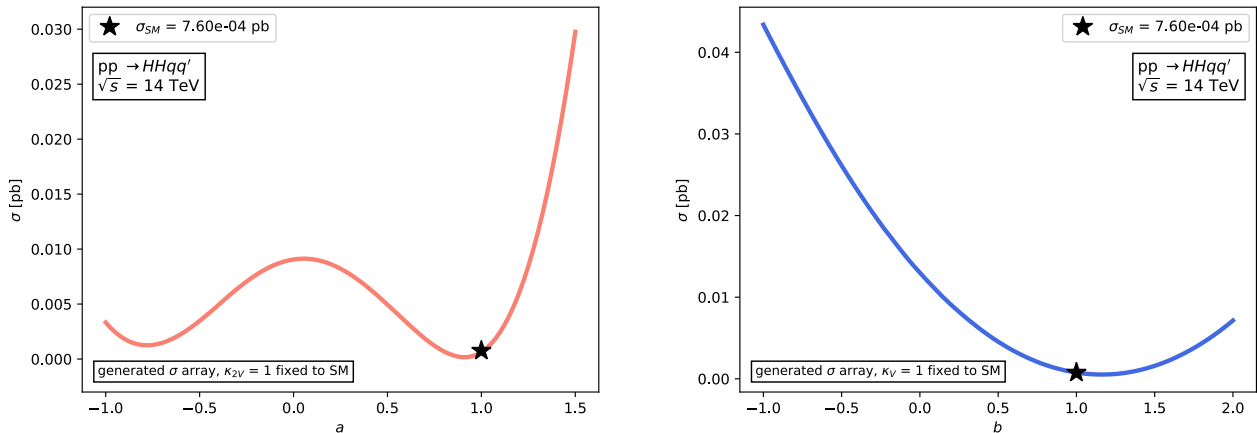


Figure 4.4. HEFT integrated cross-section of the $pp \rightarrow HHjj'$ process, $\sigma(pp \rightarrow HHjj')$, as a function of each of the two relevant parameters, either $\kappa_V = a$ [left] or $\kappa_{2V} = b$ [right]. For each graph, the parameter that is not explicit, has been fixed to the SM value, either $\kappa_{2V} = 1$ [left] or $\kappa_V = 1$ [right]. The intervals considered here are $-1 < \kappa_V < 1.5$ and $-1 < \kappa_{2V} < 2$.

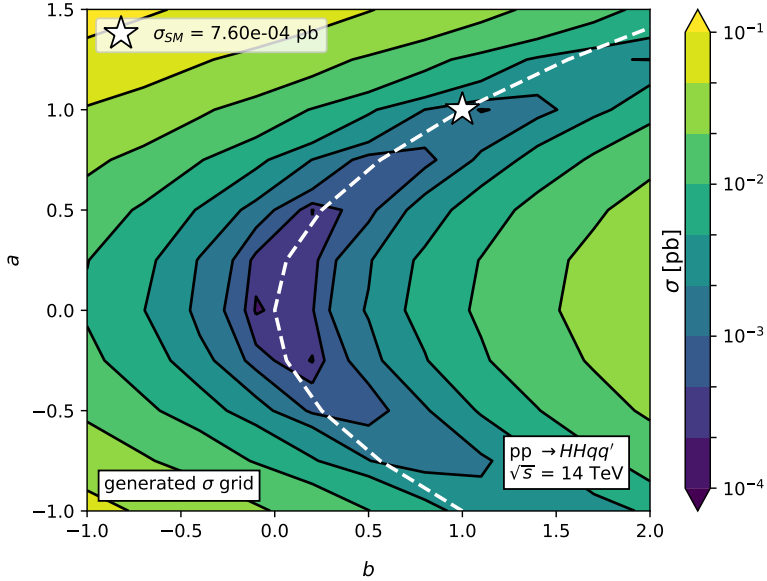


Figure 4.5. Contour lines of HEFT cross-section predictions for the HH production, $\sigma(pp \rightarrow HHjj')$, in the $(\kappa_{2V}, \kappa_V) = (b, a)$ plane. The grid consists of 121 simulations with different κ_V and κ_{2V} pairs within the intervals $-1 < \kappa_V < 1.5$ and $-1 < \kappa_{2V} < 2$. The point $\kappa_V = \kappa_{2V} = 1$ is indicated with a star and corresponds to the standard model, whose cross-section is specified in the legend. The white dashed line corresponds to all points following a $\kappa_V^2 - \kappa_{2V} = 0$ combination.

Despite the present constraints for both κ_V and κ_{2V} , and for illustrative purposes, we have considered analyzing the sensitivity of the Higgs boson pair production cross-section for a wider set of HEFT models, with κ parameters comprising the following values:

$$-1.0 < \kappa_V < 1.5, \quad -1.0 < \kappa_{2V} < 2.00 \quad (4.3)$$

Figure 4.4 shows the integrated cross-section for the $pp \rightarrow HHjj'$ process as a function of either $a = \kappa_V$ or $b = \kappa_{2V}$. Specifically, the function on the left illustrates the sensitivity of the process to a particular set of HEFT models for which the value of κ_{2V} is fixed to the SM, $\kappa_{2V} = 1$, and κ_V is left as a free parameter. The analogue for κ_{2V} is represented on the right.

The total cross-section with respect to κ_V exhibits two local minima in the considered range of values. For the cross-section with respect to κ_{2V} , there is only a minimum point. The number of local minima reflects the order of the insertions each coefficient has in the amplitude of the VBF subprocess, discussed in section 3. A quadratic dependence with a given κ in the amplitude reflects two insertions whereas a linear dependence reflects single insertions. This aspect will be relevant in future discussions throughout this subsection. Following from the κ_V insertion being of order two, the integrated cross-section with respect to κ_V exhibits an axis of symmetry at $\kappa_V \approx 0$, again associated with the leading term of the high energy expansion in the VBF amplitude. However, the local maximum does not appear exactly at $\kappa_V = 0$, and both local minima are not localized at the exact values of $\kappa_V = \pm 1$, but they are slightly shifted. Furthermore, the cross-section present at the minima at $\kappa_V < 0$ is slightly greater than the predicted value for the minima at $\kappa_V > 0$. These slight deviations from the simple behaviour found for the subprocess $A(V_L V_L \rightarrow HH)$ at high energies in eq. 3.7 reflect simply the effect of the small contributions from the next order, $\mathcal{O}(s^0)$, in the large energy expansion of this amplitude that are obviously entering in the full process computation.

On top of both distributions in Figure 4.4, the cross-section for the particular set of κ values that correspond to the SM is indicated with a starred mark. We can see in both distributions that the SM prediction is quite close to the cross-section minimum. Thus, we expect a limited sensitivity in the $pp \rightarrow HHjj'$ process to the set of HEFT models with small departures from $\kappa_V = 1$ and $\kappa_{2V} = 1$. This sensitivity is slightly greater for the κ_V distribution, as a result of the minimum having a bigger curvature.

The previous graphs offer us an insight into the role that each κ parameter has on the total cross-section of the process. However, as we mentioned in the introduction, one of the main benefits of using the HEFT formalism is the treatment of the a and b coefficients as independent parameters, in contrast to other EFTs such as the SMEFT. Figures 4.5 and 4.6 show the integrated cross-section of the $pp \rightarrow HHjj'$ process with respect to both κ_V and κ_{2V} parameters together, as contour maps over the (κ_{2V}, κ_V) parameter space. Both maps are obtained from the same calculations, but Figure 4.5 shows the total cross-section obtained from exact parton-level simulations whereas Figure 4.6 shows the approximate results from an interpolated function with a 100 times increase in the resolution. This interpolation is performed via the fitting of the set of cross-sections from each parton-level simulation to a polynomial in two variables, namely $\kappa_V \equiv a$ and $\kappa_{2V} \equiv b$. The polynomial is formed as an expansion in powers of a and b up to a^4 and b^2 as follows:

$$\sigma_{pp \rightarrow HHjj'}(a, b) = C_{a^4}a^4 + C_{a^3}a^3 + C_{a^2}a^2 + C_{a^2b}a^2b + C_{ab}ab + C_{b^2}b^2 \quad (4.4)$$

Notice that other potential combinations of coefficients have not been considered since they do not result from any interference from the different diagrams discussed in the amplitude calculation of Section 3. The resulting cross-section interpolated function is described by the following coefficients:

$$C_{a^4} = 1.62 \times 10^{-2}pb, \quad C_{a^3} = -0.41 \times 10^{-2}pb, \quad C_{a^2} = 0.05 \times 10^{-2}pb \quad (4.5)$$

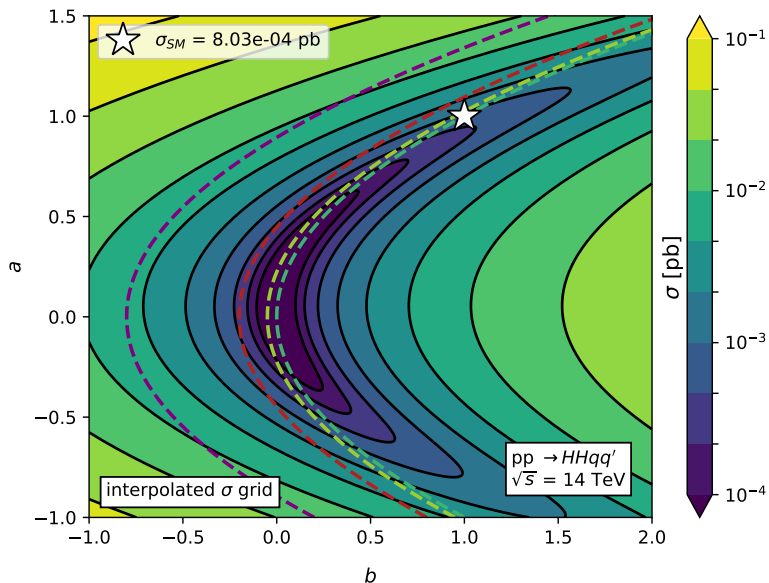


Figure 4.6. Interpolated two variable function for the integrated cross-section of the contour lines of $\sigma(pp \rightarrow HHjj')$ in the $(\kappa_{2V}, \kappa_V) = (b, a)$ plane. The considered intervals are $-1 < \kappa_V < 1.5$ and $-1 < \kappa_{2V} < 2$. The point $\kappa_V = \kappa_{2V} = 1$ is indicated with a star and corresponds to the standard model, whose cross-section is specified in the legend. The dashed lines correspond to all points following $\kappa_V^2 - \kappa_{2V} = 0.00$ [dark green], $\kappa_V^2 - \kappa_{2V} = 0.05$ [light green], $\kappa_V^2 - \kappa_{2V} = 0.20$ [red] and $\kappa_V^2 - \kappa_{2V} = 0.80$ [violet] correlations.

$$C_{a^2b} = -2.41 \times 10^{-2} pb, \quad C_{ab} = 0.26 \times 10^{-2} pb, \quad C_{b^2} = 0.93 \times 10^{-2} pb.$$

Since the coefficients C_{a^2b} , C_{ab} , and C_{a^3} are not negligible, we expect our process to be sensitive not only to the absolute value of a and b coefficients, but also to their individual and relative sign. The direction in which we move along the (κ_{2V}, κ_V) parameter space will play an important role in our analysis of the sensitivity to the $\kappa_V^2 - \kappa_{2V}$ combination. The main conclusion from the comparison of these two contour plots in Figs. 4.5 and 4.6 is that this interpolating function works pretty well and provides quite accurate predictions for the total rates of the $pp \rightarrow HHjj$ (with VBF topology) process within the HEFT models. We have also checked that this same function with the coefficients scaled down by the factor $\text{BR}(H \rightarrow b\bar{b}) \times \text{BR}(H \rightarrow \gamma\gamma)$ also works pretty well for the extrapolated events in the forthcoming analysis where we study the HEFT signal events with final state $b\bar{b}\gamma\gamma jj$.

The most important outcome from our study of the total cross section $\sigma(pp \rightarrow HHjj)$ with VBF topology in these two figures, Figs. 4.5 and 4.6, is the relevance of the value of the combination $\kappa_V^2 - \kappa_{2V}$. The larger this value is, the larger is the departure of the HEFT cross-section with respect to the SM prediction, given by:

$$\sigma_{pp \rightarrow HHjj}^{SM, a=b=1} = 8.033 \times 10^{-4} pb. \quad (4.6)$$

From a quantitative standpoint, the least sensitive region to test is the central darker region, $-0.4 < \kappa_V < 0.6$, $-0.2 < \kappa_{2V} < 0.4$, which is near the $\kappa_V^2 - \kappa_{2V} = 0$ contour line. For the particular cases studied here, we see that the largest values of the cross-section are reached for the largest values considered of $a^2 - b$ and the smallest cross-section values are reached for the smallest values of $a^2 - b$ considered, i.e., those close to the contour line $a^2 - b = 0$. In particular, the highest cross-sections, and thus sensitivities, are obtained near the point $(a, b) = (1.5, -1.0)$, with $a^2 - b = 3.25$ and with a calculated value of $\sigma^{a=1.5, b=-1.0} = 0.132$ pb, more than two orders of magnitude greater than the SM cross-section. Therefore, we can already conclude that the largest sensitivity to the κ 's is reached in the regions of the plane distant from the $(\kappa_V^2 - \kappa_{2V}) = 0$ line (dashed white line in Figure 4.5). Thus, going to a dedicated study of the sensitivity to BSM physics via the combination $(\kappa_V^2 - \kappa_{2V})$ is clearly motivated.

The most clear test that this $\kappa_V^2 - \kappa_{2V}$ combination is the most relevant parameter is provided in Fig. 4.7, where the contourlines of the cross section, $\sigma(pp \rightarrow HHjj)$, are shown differently than in the previous figures. Here, the cross-section predictions are done with the interpolating function and are displayed in the $(\kappa_V, \kappa_V^2 - \kappa_{2V}) = (a, a^2 - b)$ plane on the left plot, and on the $(\kappa_{2V}, \kappa_V^2 - \kappa_{2V}) = (b, a^2 - b)$ plane in the right plot. The ranges considered in this plot for κ_V , κ_{2V} , and $\kappa_V^2 - \kappa_{2V}$ are $-1 < \kappa_V < 1.5$, $-1 < \kappa_{2V} < 2$, and $-2 < \kappa_V^2 - \kappa_{2V} < 3.25$, respectively. Several dashed lines with particular values of $a^2 - b$ are also included for reference. Notice that in the right plot, there exists a white region where there are no predictions because it corresponds to values of $\kappa_V^2 - \kappa_{2V}$ and κ_{2V} for which κ_V results imaginary. The most important feature in these two plots is the shape found for the contourlines that are nearly flat along either κ_V or κ_{2V} axis, indicating that there is a weaker sensitivity to these two parameters when considered separately and a stronger sensitivity when combined via $\kappa_V^2 - \kappa_{2V}$.

Therefore, we conclude from this subsection that the particular combination of the HEFT a and b parameters given by $(a^2 - b)$, or, equivalently, by $(\kappa_V^2 - \kappa_{2V})$, is indeed the most relevant one to study the implications of BSM Higgs physics in the total rates of $HHjj$ production at LHC. In the next subsection, we will show that this relevance of the combination $(a^2 - b)$ also appears in the differential cross section with respect to the pseudo-rapidity of the final Higgs bosons.

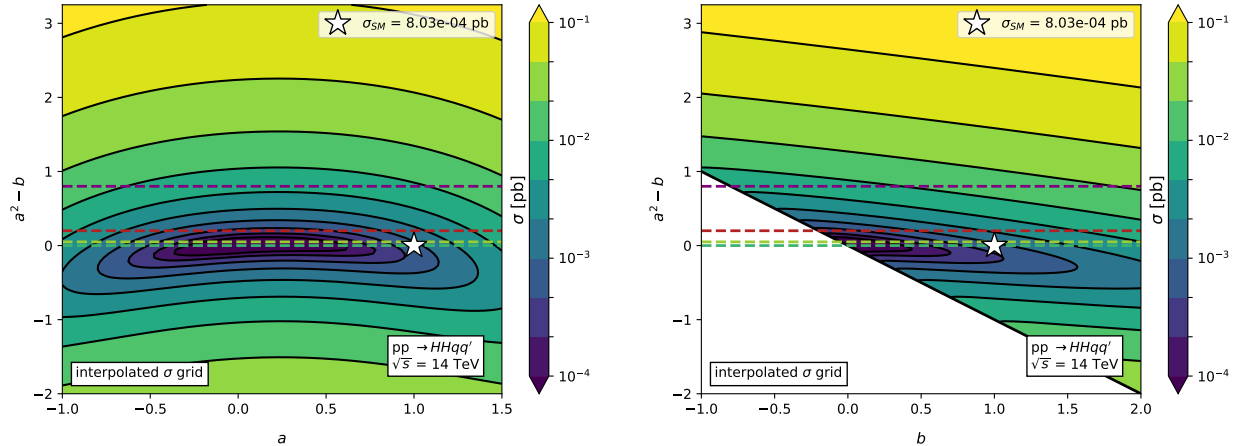


Figure 4.7. Interpolated two variable function of the contour lines of $\sigma(pp \rightarrow HHjj')$ in the $(\kappa_V, \kappa_V^2 - \kappa_{2V}) = (a, a^2 - b)$ plane [left] or $(\kappa_{2V}, \kappa_V^2 - \kappa_{2V}) = (b, a^2 - b)$ plane [right]. The considered intervals are $-1 < \kappa_V < 1.5$, $-1 < \kappa_{2V} < 2$ and $-2 < \kappa_V^2 - \kappa_{2V} < 3.25$, respectively. The SM point is indicated with a star. The dashed lines correspond to all points following $\kappa_V^2 - \kappa_{2V} = 0.00$ [dark green], $\kappa_V^2 - \kappa_{2V} = 0.05$ [light green], $\kappa_V^2 - \kappa_{2V} = 0.20$ [red] and $\kappa_V^2 - \kappa_{2V} = 0.80$ [violet] correlation parameters. The white region present in graph B corresponds to values of $\kappa_V^2 - \kappa_{2V}$ and κ_{2V} for which κ_V results imaginary.

4.3 HEFT differential cross section, $d\sigma(pp \rightarrow HHjj')/d\eta_H$, versus $(\kappa_V^2 - \kappa_{2V})$

In this subsection, we explore the HEFT predictions for some differential cross-sections that may enhance the sensitivity to the combination $(\kappa_V^2 - \kappa_{2V})$ of our interest here. In particular, we focus on the differential cross section with respect to the Higgs boson's pseudo-rapidity η_H , which turns out to be an interesting variable in this study, given the expected high transversality of the final Higgs bosons, as discussed in section 3.

In order to study the angular phenomenology of our process with respect to the aforementioned combination of κ_V and κ_{2V} , we simulated a sample consisting of 20 signals obtained using HEFT models with the particular combinations of the κ -parameters $\kappa_V^2 - \kappa_{2V} = 0.00, 0.05, 0.20$ and 0.80 .

Figure 4.8 shows the predicted differential cross-section within HEFT of the $pp \rightarrow HHjj'$ signals with respect to the pseudo-rapidity η_{H_1} of the Higgs boson leading in P_T . Each of the four lines included within each graph are obtained using a HEFT model with a different value for the $\kappa_V^2 - \kappa_{2V}$ combination. Signals in dark green correspond to $\kappa_V^2 - \kappa_{2V} = 0.00$, in light green to $\kappa_V^2 - \kappa_{2V} = 0.05$, in red to $\kappa_V^2 - \kappa_{2V} = 0.20$, and in violet to $\kappa_V^2 - \kappa_{2V} = 0.80$. The title of each graph also indicates explicitly the value of the a or b parameter fixed for all four lines. Predictions obtained using the values $a = b = 1$ corresponding to the SM case are shown in black.

We put our focus first on the first plot ($\kappa_V = 1.00$) and the fourth plot ($\kappa_{2V} = 1.00$) since both plots include the SM prediction and we can compare this reference case with the HEFT predictions. Using HEFT models with increasing values for the combination parameter $\kappa_V^2 - \kappa_{2V}$, the BSM signals deviate from the SM twin-peak distribution to a central distribution with respect to the Higgs pseudo-rapidity. These twin-peak distributions with maxima at $|\eta_H| \approx 2$ characteristic of the SM are associated typically with the VBF topology. Moreover, we see clearly that the height of the central peak around $\eta_H = 0$ in the HEFT predictions grows with the value of $(\kappa_V^2 - \kappa_{2V})$, as expected from the commented behaviour of the subprocess amplitude \mathcal{A}_L with this combination of HEFT parameters.

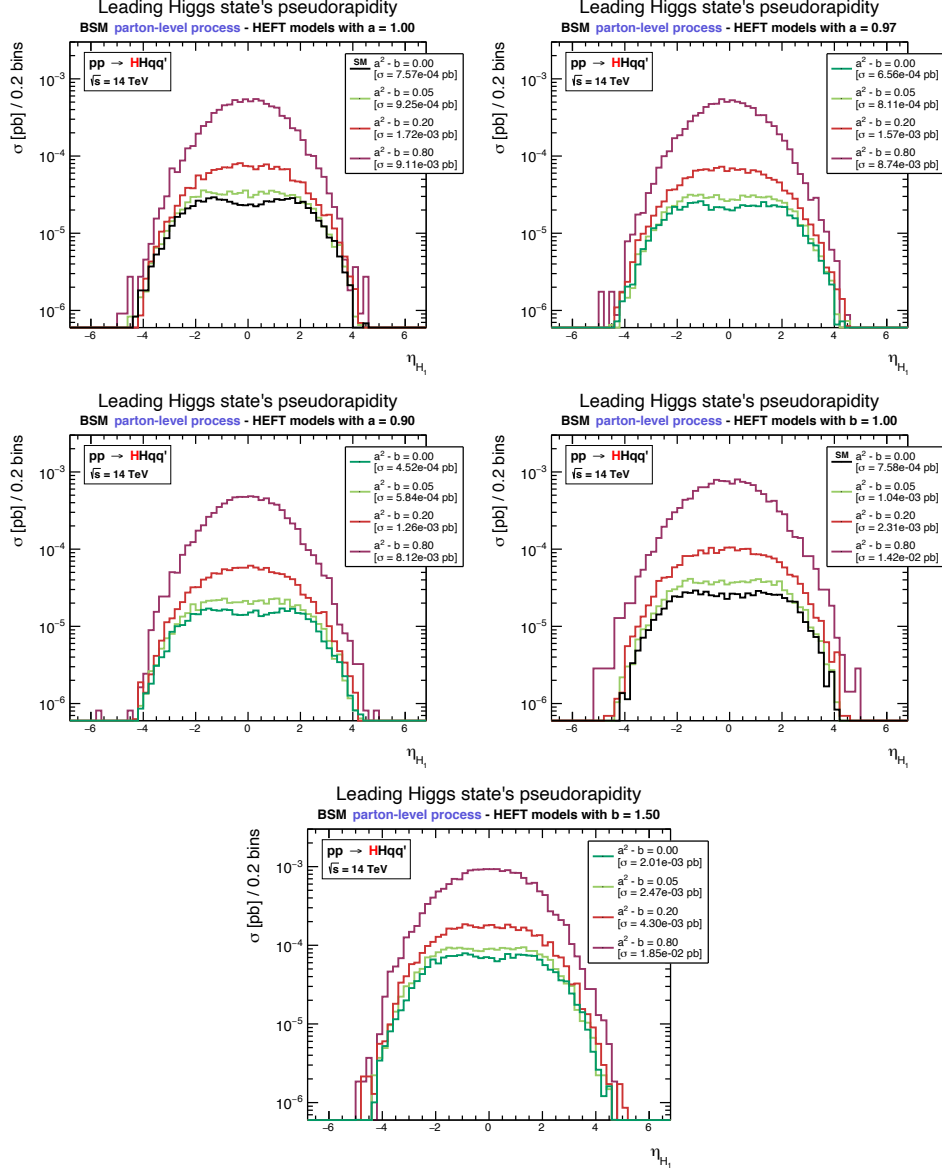


Figure 4.8. Parton level HEFT predictions for the differential cross-section of the $pp \rightarrow HHjj'$ process with respect to the pseudo-rapidity of the Higgs boson leading in P_T , $d\sigma(pp \rightarrow HHjj')/d\eta_{H_1}$, for different values of a and b parameters. Each line's color corresponds to a given value of the combination $(a^2 - b)$: $(a^2 - b) = 0.00$ [dark green], $(a^2 - b) = 0.05$ [light green], $(a^2 - b) = 0.20$ [red] and $(a^2 - b) = 0.80$ [violet]. The parameter fixed for each graph, either $a = \kappa_V$ or $b = \kappa_{2V}$, is indicated in the title of each plot. Specifically, from top to bottom, left to right, the choices are $a = 1.00$, $a = 0.97$, $a = 0.9$, $b = 1.00$, $b = 1.50$. Distributions in black correspond to SM ($a = b = 1$) predictions.

In Fig. 4.8, we also see that all HEFT predictions with a null value for the combination parameter $\kappa_V^2 - \kappa_{2V} = 0.00$ have the same exact twin-peak η_{H_1} shape as that of the SM. Therefore, the difference between HEFT models in the angular phenomenology of the Higgs bosons is mainly determined by this combination parameter. The only visible difference between HEFT predictions with the same value for the combination parameter $\kappa_V^2 - \kappa_{2V}$ is the height of the distribution, originating exclusively from the fact that cross-sections are different for each signal, as discussed in Subsection 4.2. Generally, higher

value for the κ parameters, such as $\kappa_{2V} = 1.50$ lead to higher cross sections, present in the border of the contour map of figure 4.6. As an example, the violet ($\kappa_V^2 - \kappa_{2V} = 0.80$) signal on the third graph ($\kappa_V = 0.90$) has half the total cross-section of the equivalent present on the fifth graph ($\kappa_{2V} = 1.50$).

Therefore, exploring the differential cross section with respect to the Higgs boson pseudo-rapidity and looking for the HEFT enhancements in the surrounding region close to the central peaks at $\eta_H = 0$ seems to offer a good discriminant to disentangle the BSM physics with the highest sensitivity via the combination parameter ($\kappa_V^2 - \kappa_{2V}$) $\neq 0$. As we will see in the following sections, these same features will manifest when moving to the realistic final state $pp \rightarrow HHjj \rightarrow b\bar{b}\gamma\gamma jj'$, even after including showering and detector effects.

5 Detector-level HEFT prospects for $pp \rightarrow HHjj \rightarrow b\bar{b}\gamma\gamma jj'$

In the following, we show the HEFT predictions for the total cross section and differential cross sections as a function of ($\kappa_V^2 - \kappa_{2V}$), once showering, hadronization and detector level effects are taken into account, considering the realistic final state with two b-jets, two light jets, and two photons. The total process that will be studied here is $pp \rightarrow HHjj \rightarrow b\bar{b}\gamma\gamma jj'$, which is produced from the previously studied $HHjj$ case after the two final Higgs bosons decay to $H \rightarrow b\bar{b}$ and $H \rightarrow \gamma\gamma$, respectively.

For a realistic study, jets at the final state are properly defined considering not only parton showering and hadronization phenomena, but also the clustering techniques leading to the definition of the jets from the results of the hadron fragmentation. Thus, instead of the partonic level process, $pp \rightarrow b\bar{b}\gamma\gamma q_1 q_2$, one must consider $pp \rightarrow j_b j_{\bar{b}} \gamma\gamma jj'$, with $j_b j_{\bar{b}}$ the two “true” b-jets and $\gamma\gamma$ the two “true” photons from the HH pair decay, and jj' the two “true” light jets characterizing the VBF topology. Parton showering, hadronization, and the jet clustering process are implemented on top of the original MG5 parton-level simulations using PYTHIA8.235 [19]. In particular, the algorithm used to perform the clustering process is the anti- k_t [37] algorithm, implemented using the FastJet [38] package. As stated in the introduction, the Phase-2 upgraded CMS detector [21] will be simulated using DELPHES [20] for a fast and parametric detector simulation. The result of the implementation of PYTHIA constitutes an intermediate step used in combination with DELPHES to produce detector-level simulated signals.

5.1 Detector-level SM prospects for the $b\bar{b}\gamma\gamma jj'$ final state

As a reference case, we first analyze the efficiency loss when moving from parton level to detector level in the SM case (remember that the SM can be considered as a particular HEFT case with $a = b = 1$). Concretely, we start with the SM sample that we have generated at the parton level, as already outlined in table 4.2. This selected sample is then passed through PYTHIA and DELPHES imposing additional selection criteria, as specified in table 5.1.

The selection efficiency used to evaluate each individual criterion i is defined as:

$$E_i = N_{i \text{ detector-level}} / N_{\text{parton-level}} \quad (5.1)$$

where $N_{i \text{ detector-level}}$ denotes the number of events resulting from the detector-level selection criterion i applied to the initial $N_{\text{parton-level}}$ parton-level events. Table 5.1 shows the selection efficiencies resulting from the application of each selection criterion to the SM sample. It is worth noting that, for consistency reasons, the detector-level selection strategy for the VBF topology is similar to the event selection present

Detector-level event selection strategy for the SM case		
		SM Selection efficiencies (E_i)
VBF topology	At least two light jets with: $P_{T,j} > 20$ GeV, $2 < \eta_j < 5$	66%
	Selected VBF jet pair jj' maximizes the ΔR between light jets	
	VBF jets with: $\eta_j \times \eta_{j'} < 0$	91%
	VBF jet pair with: $m_{jj'} > 500$ GeV	98%
HH topology	At least two loosely identified photons with $P_{T,\gamma} > 18$ GeV, $ \eta_\gamma < 2.5$	86%
	Selected photon pair $\gamma\gamma$ maximizes proximity to $m_{\gamma\gamma} = m_H = 125$ GeV	
	At least two loosely b-tagged jets with $P_{T,j_b} > 25$ GeV, $ \eta_{j_b} < 2.5$	81%
	Selected b -jet pair $j_b j_{\bar{b}}$ maximizes proximity to $m_{j_b j_{\bar{b}}} = m_H = 125$ GeV	
Total selection efficiency $\Pi^i E_i$		36%

Table 5.1. Detector-level event selection strategy for the SM case with $b\bar{b}\gamma\gamma jj'$ final state

at the parton level, outlined in table 4.2. For the photon and the b-tagged jet definitions at detector level, we have considered a “loose” working point from the preestablished DELPHES options. According to [39] this “loose” working point is defined as that presenting an efficiency in the identification/tagging of a photon of 90% and a b-jet of 90%. The combination of all selection efficiencies is then defined as the product of the individual efficiencies $\Pi^i E_i$, which is also shown in this table.

Some comments are in order for the various selection criteria. The selected events in the first criterion are required to have a minimum of two light jets with $P_{T,j} > 20$ GeV and $2 < |\eta_j| < 5$. This criterion also includes the requirement that the selected two light jets maximize the distance ΔR between them. The resulting selection efficiency is $E_1 = 66\%$ for the SM signal (and close to $E_1 \approx 65\%$ for all studied BSM signals). This criterion is the one contributing the most to the selection efficiency loss. The selected VBF jet pair is required to have an invariant mass greater than $m_{jj'} > 500$ GeV and both light jets to have a pseudo-rapidity with opposed sign. These two requirements have a general selection efficiency close to $E_2 \approx E_3 \approx 95\%$. The combination of the selection efficiencies from the detector-level VBF topology selection is, in general, of approximately a $E_1 \times E_2 \times E_3 \approx 60\%$ and dominates the selection efficiency loss at detector-level. Aside from the VBF selection process, the selected events are required to have a pair of reconstructed photons and b -jets satisfying the following set of criteria. The selected events are required to have a minimum of 2 b-tagged jets with $P_T > 25$ GeV and $|\eta| < 2.5$ and a minimum of two photons with $P_T > 18$ GeV and $|\eta| < 2.5$. For all studied signals, the selection efficiency of both sets of criteria is close to a $E_4 \approx E_5 \approx 80\%$ respectively. In summary, For the particular case of the SM sample, the application of the selection strategy in Table 5.1 at detector level results in a combined selection efficiency value of $(\Pi^i E_i)^{SM} = 36\%$, that is, a reduction of approximately 1/3 of the predicted amount of events produced at parton level. It is important to note that the value of $\Pi^i E_i$ is not yet fully optimized at this point. We will investigate later a better optimized choice of selection criteria when studying together the HEFT signal and the background events in the last section.

Regarding the efficiency loss in the SM differential cross-section distributions we have studied several

$a = 1.00$								
$a^2 - b$	-1.00	-0.80	0.00 (SM)	0.05	0.20	0.80	1.00	1.50
$\sigma[pb]$	$1,25 \times 10^{-5}$	$7,66 \times 10^{-6}$	$9,54 \times 10^{-7}$	$1,22 \times 10^{-6}$	$2,49 \times 10^{-6}$	$1,49 \times 10^{-5}$	$2,17 \times 10^{-5}$	$4,39 \times 10^{-5}$
$\Pi^i E_i$	44%	44%	36%	36%	39%	41%	41%	43%
N	16	10	1.0	1.3	2.9	18	27	56

$a = 0.97$				$a = 0.90$				
$a^2 - b$	0.00	0.05	0.20	0.80	0.00	0.05	0.20	0.80
$\sigma[pb]$	$8,12 \times 10^{-7}$	$1,06 \times 10^{-6}$	$2,28 \times 10^{-6}$	$1,44 \times 10^{-5}$	$5,55 \times 10^{-7}$	$7,55 \times 10^{-7}$	$1,85 \times 10^{-6}$	$1,34 \times 10^{-5}$
$\Pi^i E_i$	36%	36%	38%	41%	35%	37%	38%	42%
N	0.87	1.1	2.6	18	0.58	0.84	2.1	17

kinematic variables of interest for the final state, $b\bar{b}\gamma\gamma jj'$. In particular, we have considered: invariant mass of the photon pair $M_{\gamma\gamma}$, invariant mass of the b -jet pair $M_{b\bar{b}}$, invariant mass of the light jet pair $M_{j_1 j_2}$, pseudo-rapidity of the light jet with P_T leading $\eta_{j_1}^{\text{leading}}$, pseudo-rapidity difference between both light jets $\Delta\eta_{j_1, j_2}$, invariant mass of the system with two photons and two b -jets $M_{\gamma\gamma b\bar{b}}$, transverse momentum of the photon pair $P_{T, \gamma\gamma}$, pseudo-rapidity of the photon pair $\eta_{\gamma\gamma}$, transverse momentum of the b -jet pair, $P_{T, b\bar{b}}$, and pseudo-rapidity of the b -jet pair $\eta_{b\bar{b}}$. As a general conclusion, we have checked that most of the distributions do not show relevant changes in their shape, comparing them to the original parton-level distributions. In particular, in the cases of angular variables there is no appreciable change in the filtered distributions after PYTHIA and DELPHES respect to the parton-level ones. This is clearly the case of the distributions in pseudo rapidity and in transverse momentum variables. The most relevant change occurs in the distributions with $M_{\gamma\gamma}$ and $M_{b\bar{b}}$, as expected. The efficiency loss introduced by the hadronization, showering and detector effects are therefore noticed at the total cross section level and not so much at the differential cross section level. A similar conclusion will show up in the HEFT predictions as will be presented in the next subsection.

5.2 Detector-level BSM prospects within the HEFT for the $b\bar{b}\gamma\gamma jj'$ final state

In this subsection, we analyze the efficiency loss when moving from parton level to detector level in the HEFT case with different values for the a and b coefficients other than those of the SM case, i.e. , for $a \neq 1$ and/or $b \neq 1$. We focus our analysis on the HEFT predictions for the various corresponding values of the combination of our interest $a^2 - b$. As in the previous case, we start with the HEFT sample that we have generated at the parton-level, as already outlined in table 4.2. This selected HEFT sample is then passed through PYTHIA and DELPHES imposing additional selection criteria, as already specified for the SM in table 5.1. We summarize the HEFT results in tables 5.2 and 5.3. These tables include the HEFT predictions for the parton-level integrated total cross section, $\sigma(b\bar{b}\gamma\gamma jj')$, the total efficiency loss $\Pi^i E_i$, and the total number of events N using a prospected integrated luminosity of 3000 fb^{-1} as one of the benchmarks for the HL-LHC operation [40].

Table 5.2 gathers the combined selection efficiency values and the predicted integrated number of events for each of the analyzed BSM signals. Four extra BSM signals obtained from HEFT $a = 1$ have been included for reasons of completeness, which feature high positive or negative values of the parameter combination $\kappa_V^2 - \kappa_{2V}$.

$a^2 - b$	$b = 1.00$				$b = 1.50$			
	0.00 (SM)	0.05	0.20	0.80	0.00	0.05	0.20	0.80
$\sigma[pb]$	$9,47 \times 10^{-7}$	$1,36 \times 10^{-6}$	$3,34 \times 10^{-6}$	$2,24 \times 10^{-5}$	$2,64 \times 10^{-6}$	$3,33 \times 10^{-6}$	$6,07 \times 10^{-6}$	$2,89 \times 10^{-5}$
$\Pi^i E_i$	35%	35%	39%	40%	36%	36%	36%	40%
N	1.0	1.4	3.9	27	2.8	3.6	6.6	34

Table 5.2. HEFT predictions for the final state $b\bar{b}\gamma\gamma jj'$ for various selections of the HEFT parameters a , b and the combination $a^2 - b$. We include the integrated parton-level cross-section, $\sigma(b\bar{b}\gamma\gamma jj')$, the combined selection efficiencies value $\Pi^i E_i$ and the expected number of events N at HL-LHC.

b	$a = 1.00$			
	3.00	2.00	0.00	-1.00
$a^2 - b$	-2.00	-1.00	1.00	2.00
$\sigma[pb]$	$5,61 \times 10^{-5}$	$1,25 \times 10^{-5}$	$2,17 \times 10^{-5}$	$7,43 \times 10^{-5}$
$\Pi^i E_i$	44%	44%	41%	43%
N	74	16	27	95

Table 5.3. HEFT predictions for the final state $b\bar{b}\gamma\gamma jj'$ as in table 5.2 but now considering other coefficients leading to larger values for the relevant combination parameter $a^2 - b$ ranging from -2 to 2.

Quantitatively, the studied BSM signals show combined selection efficiencies values in the range $35\% < \Pi^i E_i < 44\%$, therefore better than in the SM case. Higher values are obtained from HEFT signals with a higher absolute value for the $\kappa_V^2 - \kappa_{2V}$ combination. We conclude that BSM signals corresponding to HEFT models with a greater $\kappa_V^2 - \kappa_{2V}$ combination are predicted to experience a smaller selection efficiency loss compared to the SM framework. This is in agreement with previous analyses within HEFT for the $HHjj$ production at LHC, which concluded that the contribution of the VBF topologies to the total cross-section of the process is increased for HEFT signals with greater $\kappa_V^2 - \kappa_{2V}$ values [27].

Using a projected integrated luminosity of 3000 fb^{-1} as one of the benchmarks for the HL-LHC operation [40], the signal with the smallest cross-section, $\sigma^{a=0.90, a^2-b=0.00} = 1.92 \times 10^{-7} \text{ pb}$, translates into a prediction of $N^{a=0.90, a^2-b=0.00} \approx 0.58$ events. The signal corresponding to the SM, $\sigma^{a=1.00, a^2-b=0.00} = 3.41 \times 10^{-7} \text{ pb}$, translates into a prediction of $N^{a=1.00, a^2-b=0.00} \approx 1.0$ events. The signal with the greatest cross-section, $\sigma^{a=1.00, a^2-b=1.50} = 1.88 \times 10^{-5} \text{ pb}$, translates into a prediction of $N^{a=1.00, a^2-b=1.50} \approx 56$ events. BSM signals calculated from HEFT models using either $\kappa_V^2 - \kappa_{2V} = 0.00$ or 0.05 do not predict, for small deviations from $(\kappa_{2V}, \kappa_V) = (1, 1)$, a noticeable production of HH pair during the HL-LHC operation. We conclude that BSM signals which predict the observation of the $HHjj$ production at the future HL-LHC operation are associated with the set of HEFT models with κ_V and κ_{2V} values far from the $\kappa_V^2 - \kappa_{2V} = 0.00, 0.05$ contour lines within the (κ_{2V}, κ_V) parameter space, where the SM scenario is present. Taking into account the tight constraints on the κ_V value, the upper section of Table 5.2 provides the most relevant HEFT predictions among the selected BSM points for using this particular channel to constrain further the value of κ_{2V} , assuming $\kappa_V \approx 1.00$.

Finally, Table 5.3 also shows the HEFT predictions for the final state $b\bar{b}\gamma\gamma jj'$ as in table 5.2, but now considering other coefficients a and b leading to larger values for the relevant combination parameter $a^2 - b$ ranging from -2 to 2. We clearly see that all the predictions for the total cross-section, the total efficiency and the total number of events grow with the value of $a^2 - b$, as expected. The cross-section grows up to near 10^{-4} pb . The total efficiency grows up to 44%. The number of predicted $b\bar{b}\gamma\gamma jj'$ events at HL-LHC ranges between 10 and 100 for all BSM signals. As a result, we expect the future HL-LHC

operation to be capable of greatly reducing the experimental constraints on the combination $\kappa_V^2 - \kappa_{2V}$.

In the last part of this subsection, we analyze the effects of showering, hadronization, and detector level on the distributions for some selected BSM cases within the HEFT. This is shown in Figs. 5.1, 5.2, and 5.3.

Figure 5.1 shows the differential cross-section distributions with respect to the pseudo-rapidity of the detector-level photon pair, for all the selected BSM points. Figure 5.2 shows the differential cross-section distributions with respect to the pseudo-rapidity of the detector-level b -jets. Qualitatively, all graphs maintain the same distribution shapes for the pseudo-rapidity of the pair products from the Higgs boson decay as those found previously from the parton-level predictions with respect to the Higgs boson pseudo-rapidity. All plots show the central peak at vanishing pseudo-rapidity of the pair, both at $\eta_{\gamma\gamma} = 0$ and $\eta_{b\bar{b}} = 0$. Signals calculated using HEFT models with an identical value for the combination $\kappa_V^2 - \kappa_{2V}$ have nearly identical pseudo-rapidity distribution shapes, not varying so much with the separate values of κ_V and κ_{2V} . Signals calculated from HEFT models with an increased value of $\kappa_V^2 - \kappa_{2V}$ predict a higher central peak, which is obviously correlated with the high transversality of the final Higgs bosons produced as already indicated.

Figure 5.3 shows the differential cross-section distributions with respect to $M_{b\bar{b}\gamma\gamma}$, i.e., the invariant mass of the photons and b -jets combined system at detector-level. From these plots we see that HEFT distributions with higher values of $\kappa_V^2 - \kappa_{2V}$ have higher rates. Also the tails at large invariant mass, $M_{b\bar{b}\gamma\gamma}$, are higher and longer as the combination parameter $\kappa_V^2 - \kappa_{2V}$ increases. This shape at detector level is equivalent to the M_{HH} distribution shape that is predicted at the parton level, as expected. Therefore, in general, the enhancement of rates at large invariant mass $M_{\gamma\gamma b\bar{b}}$ can also be used as good discriminants among BSM and SM, and when compared them to the background rates could provide an increasing sensitivity to the combination parameter $\kappa_V^2 - \kappa_{2V}$.

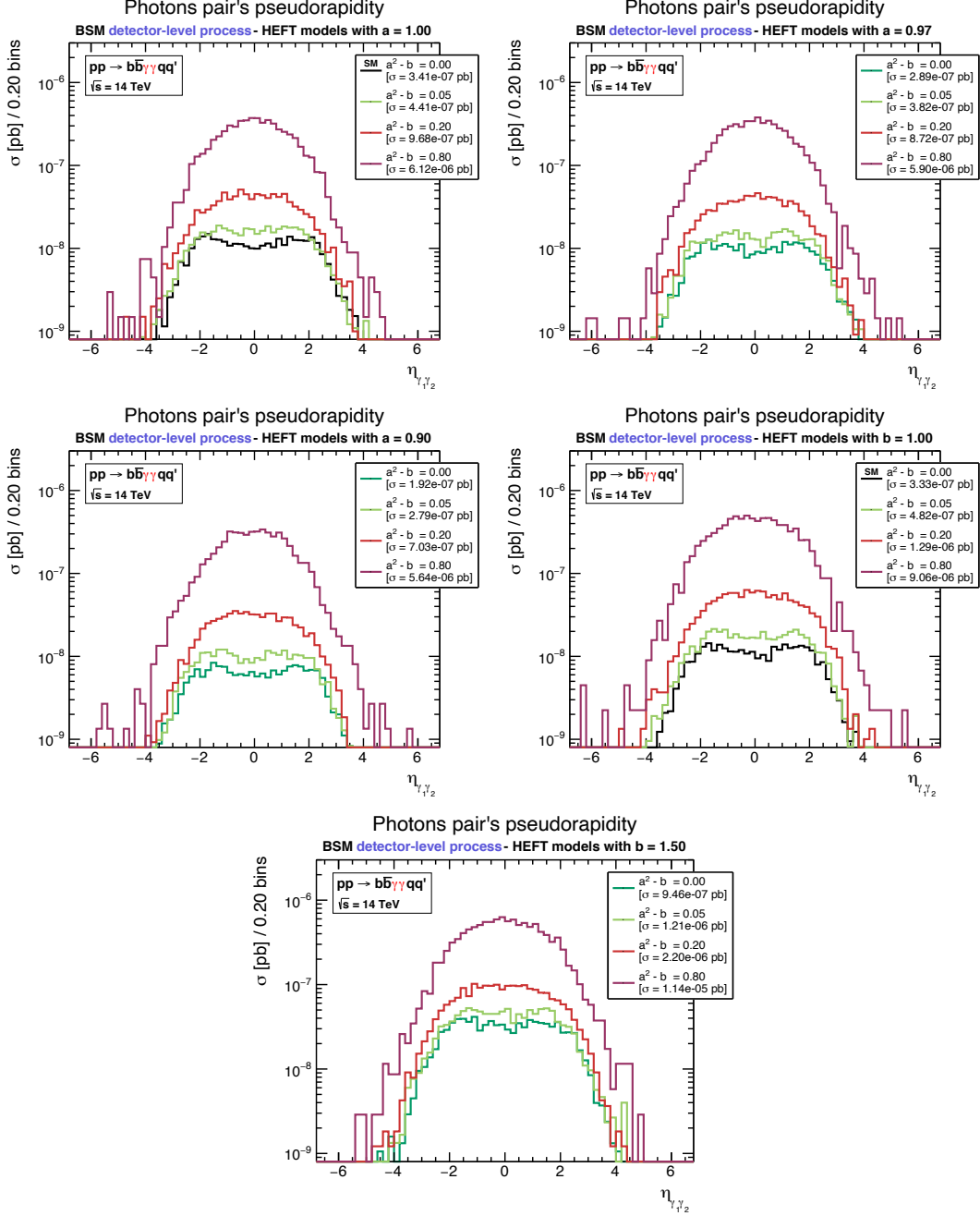


Figure 5.1. HEFT detector-level predictions for the differential cross-section of the $pp \rightarrow HHjj' \rightarrow b\bar{b}\gamma\gamma jj'$ process with respect to the photon pair pseudo-rapidity, $d\sigma(pp \rightarrow b\bar{b}\gamma\gamma jj')/d\eta_{\gamma\gamma'}$, for different values of a and b parameters. Each line's color corresponds to a given value of the combination $(a^2 - b)$: $(a^2 - b) = 0.00$ [dark green], $(a^2 - b) = 0.05$ [light green], $(a^2 - b) = 0.20$ [red] and $(a^2 - b) = 0.80$ [violet]. The parameter fixed for each graph, either $a = \kappa_V$ or $b = \kappa_{2V}$, is indicated in the title of each plot. Specifically, from top to bottom, left to right, the choices are $a = 1.00$, $a = 0.97$, $a = 0.9$, $b = 1.00$, $b = 1.50$. Distributions in black correspond to SM ($a = b = 1$) predictions.

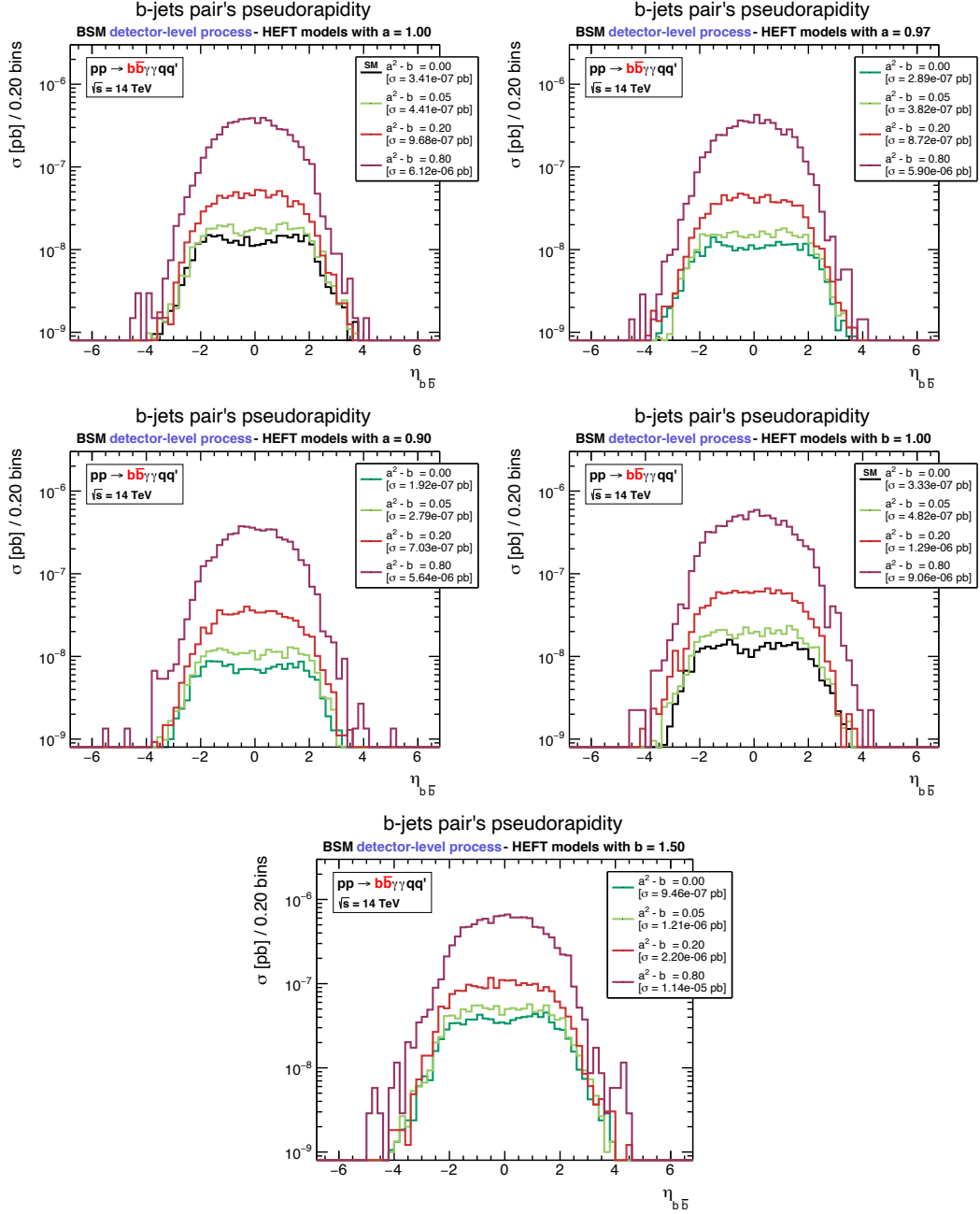


Figure 5.2. HEFT detector-level predictions for the differential cross-section of the $pp \rightarrow HHjj' \rightarrow b\bar{b}\gamma\gamma jj'$ process with respect to the b -jet pair pseudo-rapidity, $d\sigma(pp \rightarrow b\bar{b}\gamma\gamma jj')/d\eta_{b\bar{b}}$, for different values of a and b parameters. Each line's color corresponds to a given value of the combination $(a^2 - b)$: $(a^2 - b) = 0.00$ [dark green], $(a^2 - b) = 0.05$ [light green], $(a^2 - b) = 0.20$ [red] and $(a^2 - b) = 0.80$ [violet]. The parameter fixed for each graph, either $a = \kappa_V$ or $b = \kappa_{2V}$, is indicated in the title of each plot. Specifically, from top to bottom, left to right, the choices are $a = 1.00$, $a = 0.97$, $a = 0.9$, $b = 1.00$, $b = 1.50$. Distributions in black correspond to SM ($a = b = 1$) predictions.

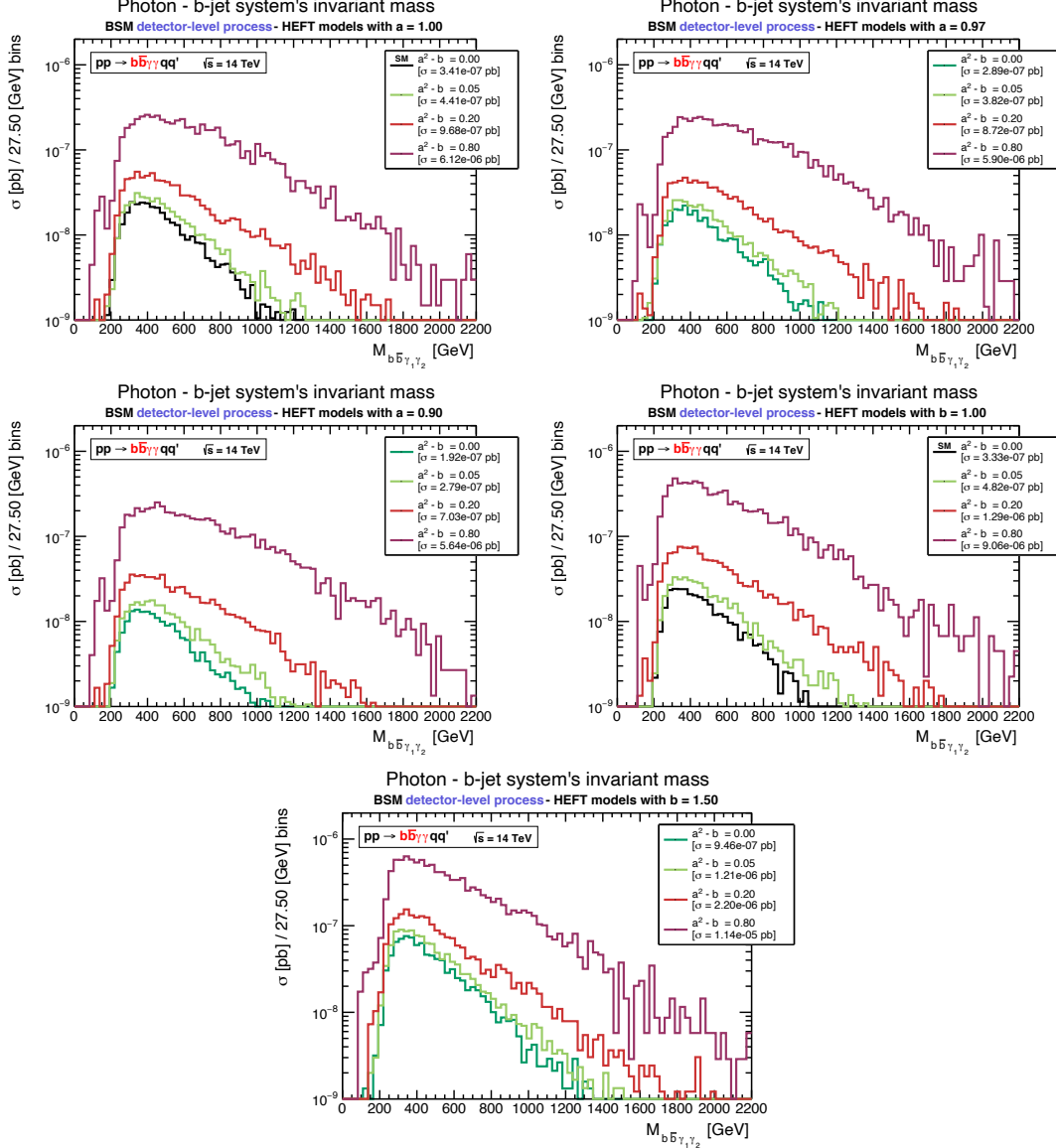


Figure 5.3. HEFT detector-level predictions for the differential cross-section of the $pp \rightarrow HHjj' \rightarrow b\bar{b}\gamma\gamma jj'$ process with respect to the invariant mass of the combined $b\bar{b}\gamma\gamma$ system, $d\sigma(pp \rightarrow b\bar{b}\gamma\gamma jj')/dM_{b\bar{b}\gamma\gamma}$, for different values of a and b parameters. Each line's color corresponds to a given value of the combination $(a^2 - b)$: $(a^2 - b) = 0.00$ [dark green], $(a^2 - b) = 0.05$ [light green], $(a^2 - b) = 0.20$ [red] and $(a^2 - b) = 0.80$ [violet]. The parameter fixed for each graph, either $a = \kappa_V$ or $b = \kappa_{2V}$, is indicated in the title of each plot. Specifically, from top to bottom, left to right, the choices are $a = 1.00$, $a = 0.97$, $a = 0.9$, $b = 1.00$, $b = 1.50$. Distributions in black correspond to SM ($a = b = 1$) predictions.

6 Sensitivity to $(\kappa_V^2 - \kappa_{2V})$ in $b\bar{b}\gamma\gamma jj'$ events from $HHjj$ production at HL-LHC

In this section we finally evaluate the expected sensitivity to the combination parameter of our interest $\kappa_V^2 - \kappa_{2V}$ in $b\bar{b}\gamma\gamma jj'$ events from $HHjj$ production at HL-LHC. For this evaluation we first compare the signal rates from the BSM events given by the HEFT for several choices of $a^2 - b$ and the background rates from the most relevant SM processes producing the same final state $b\bar{b}\gamma\gamma jj'$. This first evaluation is done at the parton-level and the results are shown in table 6.1. The three selected background processes to be compared with the BSM signal with $a^2 - b \neq 0$ are: 1) SM-EW $\gamma\gamma b\bar{b}jj$ via $HHjj$ (i.e. for $a = b = 1$, tree level) 2) SM-QCD-EW $\gamma\gamma b\bar{b}jj$ non-resonant (tree level, $\mathcal{O}(\alpha_s^2 \alpha^1 \hbar^0)$), 3) SM-QCD-EW $\gamma\gamma b\bar{b}jj$ via HH from gluon-gluon fusion (one-loop, $\mathcal{O}(\alpha_s^2 \alpha^3 \hbar^1)$), and 4) SM-EW $\gamma\gamma b\bar{b}jj$ via $ZHjj$ (tree level). These rates are all generated with MG5 and the specific cuts for each process are also included. In the background case 3) we have performed the calculation using the large m_t limit that provides a rough estimate for the most important contributions coming from the top loops. We have used an effective approach to describe the $ggHH$ effective vertex in this large m_t limit, which is $\mathcal{O}(\hbar^1)$, following Refs. [41, 42]. According to Ref. [42] this rough estimate provides larger $HHjj$ rates compared to the exact computation by a factor of up to 2-3 mainly in large invariant mass M_{HH} region, although other distributions are not so much affected. Using MG5 with this $ggHH$ effective interaction we have then generated to order $\mathcal{O}(\alpha_s^2 \alpha^3 \hbar^1)$ the final $b\bar{b}\gamma\gamma jj'$ events. Our simple estimate of this background being larger than the expected full one is therefore a conservative estimate. The most important conclusion from table 6.1 is that the most relevant background among the four selected ones is by far the second one, i.e. SM-QCD-EW $\gamma\gamma b\bar{b}jj$ non-resonant, which overpasses the others by several orders of magnitude. The starting parton-level cross section for this process is 8.1×10^{-4} pb to be compared with our BSM signal from the HEFT models which is below 10^{-4} pb. In the following we will take just this dominant background and we will explore for specific and more optimal strategies to enhance the sensitivity to our BSM signal with $a^2 - b \neq 0$. From now on we will perform our estimates of both the signal and the background at the detector level, i.e. , all the forthcoming predictions are generated with MG5 and passed through PYTHIA and DELPHES.

$\sigma(\gamma\gamma b\bar{b}jj)$ (pb): BSM signal versus SM background rates (parton level)					
Cuts applied: $p_{T_j} \geq 20$ GeV, $2 < \eta_j < 5$, $\eta_{j_1} \cdot \eta_{j_2} < 0$, $\Delta R_{jj} > 0.4$, $M_{jj} > 500$ GeV					
Additional cuts in SM-QCD-EW (non resonant) background: $M_{b\bar{b}} > 100$ GeV, $M_{\gamma\gamma} > 100$ GeV					
BSM Signal ($a^2 - b \neq 0$) $\gamma\gamma b\bar{b}jj$ via $HHjj$		SM-EW ($\mathcal{O}(\alpha^3 \hbar^0)$) $\gamma\gamma b\bar{b}jj$ via $HHjj$	SM-QCD-EW ($\mathcal{O}(\alpha_s^2 \alpha^1 \hbar^0)$) $\gamma\gamma b\bar{b}jj$ (non-resonant)	SM-QCD-EW ($\mathcal{O}(\alpha_s^2 \alpha^3 \hbar^1)$) $\gamma\gamma b\bar{b}jj$ via HH from ggF	SM-EW ($\mathcal{O}(\alpha^3 \hbar^0)$) $\gamma\gamma b\bar{b}jj$ via $ZHjj$
$a^2 - b$ ($a = 1$)					
0.2	2.2×10^{-6}	9.8×10^{-7}	8.1×10^{-4}	4.7×10^{-7}	3.6×10^{-8}
0.8	1.2×10^{-5}				
1	2.2×10^{-5}				
-1	7.4×10^{-5}				

Table 6.1. Cross section, $\sigma(\gamma\gamma b\bar{b}jj)$ (pb), at parton level: BSM rates within HEFT versus SM backgrounds rates.

In order to find the proper selection of cuts that optimizes the signal versus background rates we have designed the following strategy. First we select the events with VBF topology and require also some basic cuts for the HH topology. This is called in short Selection A VBF. Then with this selected events we study the most relevant differential cross section distributions and compare the HEFT predictions for various values of the combination parameter $(\kappa_V^2 - \kappa_{2V})$ with the dominant SM-QCD-EW (non-resonant) background. This will lead us to the proper variables to discriminate among signal and background. With these optimal variables we will then design the final strategy to enhance the sensitivity to $(\kappa_V^2 - \kappa_{2V})$ which is our main objective in this work.

In table 6.2 we summarize the cuts applied to the generated $b\bar{b}\gamma\gamma jj'$ events that define Selection A VBF and display their corresponding efficiencies for the cases SM-EW and SM-QCD-EW (non-resonant). The total (product) efficiencies are also included.

Selection A VBF:

		SM E_i	$b\bar{b}\gamma\gamma jj$ BKG E_i
VBF topology	At least two jets with: $P_{T,j} > 20$ GeV, $2 < \eta_j < 5$		
	Selected VBF jet pair jj' maximizes the ΔR between light jets	66%	62%
	VBF jets with: $\eta_j \times \eta_{j'} < 0$	91%	81%
	VBF jet pair with: $m_{jj'} > 500$ GeV	98%	93%
HH topology	At least two loosely identified photons with $P_{T,\gamma} > 18$ GeV, $ \eta_\gamma < 2.5$		
	Take the two photons $\gamma\gamma$ with the greatest P_T	79%	77%
	At least two loosely b-tagged jets with $P_{T,j_b} > 25$ GeV, $ \eta_{j_b} < 2.5$		
	Take the two b-jets $b\bar{b}$ with the greatest P_T	76%	79%
Total selection efficiency ($\prod^i E_i$)		36%	28%

Table 6.2. Cuts applied to the selected $b\bar{b}\gamma\gamma jj'$ final state defining Selection A VBF and their corresponding efficiencies for the cases SM-EW and SM-QCD-EW (non-resonant)

In figure 6.1 we compare the predictions of the selected differential cross sections for BSM signals from HEFT models with the predictions for the dominant SM-QCD-EW (non-resonant) background, all after applying Selection A VBF which is defined in table 6.2. Each panel shows a particular differential cross section with respect to the chosen kinematical variable of the $b\bar{b}\gamma\gamma j_1 j_2$ final state. The selected kinematical variables are, respectively, $p_T^{j_1 j_2}$, $M_{j_1 j_2}$, η_{j_1} , $\eta_{j_1 j_2}$, $M_{b\bar{b}\gamma\gamma}$, $P_T^{b\bar{b}\gamma\gamma}$, $\eta_{\gamma\gamma}$, $\eta_{b\bar{b}}$, $P_T^{\gamma\gamma}$, $P_T^{b\bar{b}}$, $M_{\gamma\gamma}$, $M_{b\bar{b}}$. In the BSM signals we have chosen three values of $a^2 - b = 2$, $a^2 - b = 0.8$ and $a^2 - b = 0$, for comparison. Notice that the later HEFT case (black lines) corresponds to the SM case (with $a = b = 1$).

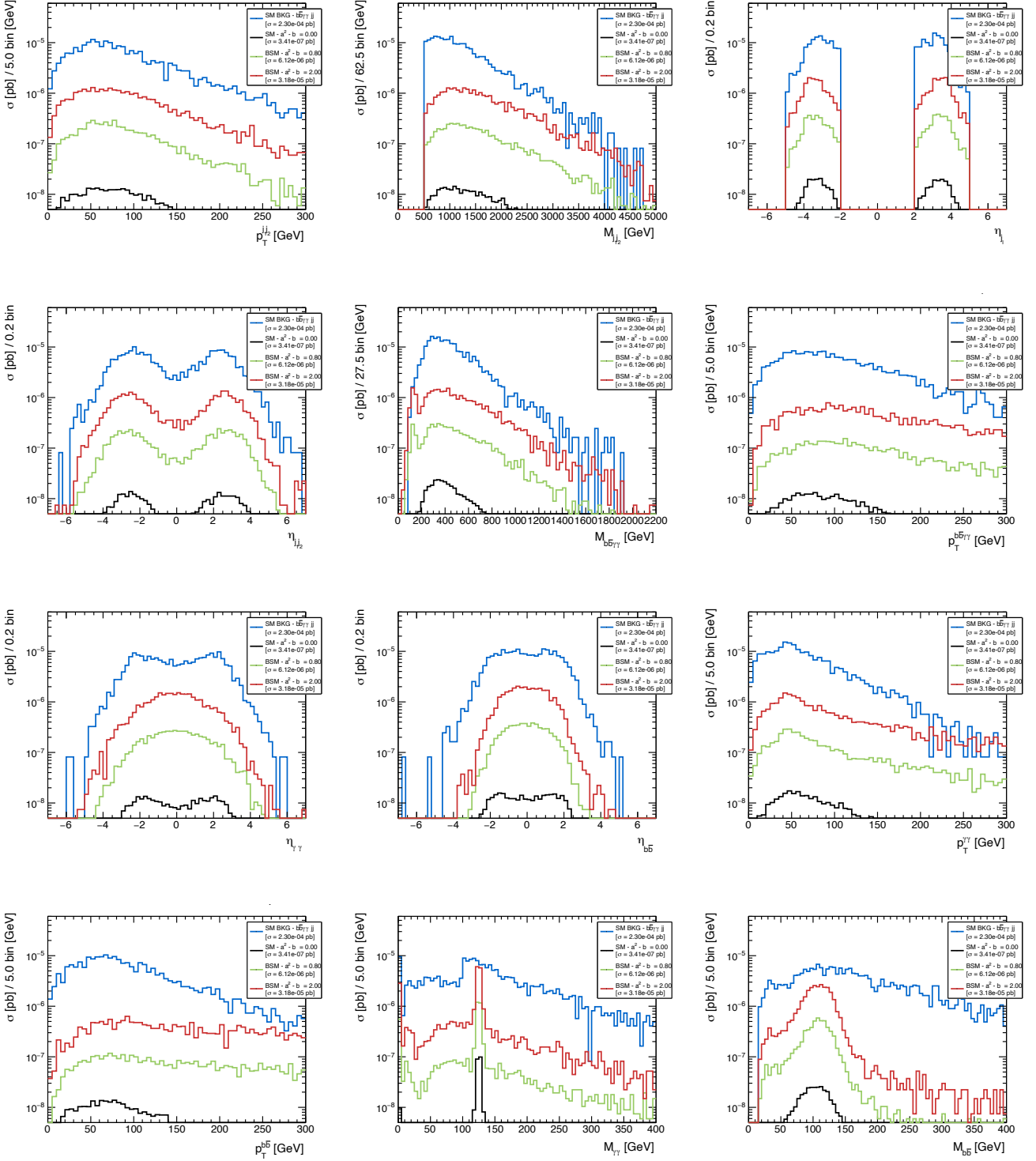


Figure 6.1. Comparison of the BSM signals from HEFT models and the dominant SM-QCD-EW (non-resonant) background after applying Selection A VBF, defined in table 6.2. Each panel shows a particular differential cross section with respect to the chosen kinematical variable of the $b\bar{b}\gamma\gamma j_1 j_2$ final state. These chosen variables are, respectively, $p_T^{j_1 j_2}$, $M_{j_1 j_2}$, η_{j_1} , $\eta_{j_1 j_2}$, $M_{b\bar{b}\gamma\gamma}$, $P_T^{b\bar{b}\gamma\gamma}$, $\eta_{\gamma\gamma}$, $\eta_{b\bar{b}}$, $P_T^{\gamma\gamma}$, $P_T^{b\bar{b}}$, $M_{\gamma\gamma}$, $M_{b\bar{b}}$. The coloured lines are the predictions for: SM-QCD-EW (non-resonant) background (light blue), HEFT signal for $a^2 - b = 2$ (red) (obtained with $(a, b) = (1, -1)$), HEFT signal for $a^2 - b = 0.8$ (green) (obtained with $(a, b) = (1, 0.2)$), HEFT signal for $a^2 - b = 0$ (black) (obtained with $(a, b) = (1, 1)$ which corresponds to the SM-EW case).

Some comments on these distributions of Fig. 6.1 are in order. First, we see that in all the panels the predictions for the dominant SM-QCD-EW (non-resonant) background (blue lines) are above the HEFT signals (red, green and black lines), as already manifested for the total parton-level cross sections in table 6.1. Second, the plots showing the largest differences in the shapes between signal and background are those for the variables of the pairs $\gamma\gamma$ and $b\bar{b}$. Specifically, these are the transverse momentum, the pseudo-rapidity and the invariant mass, i.e., $P_T^{b\bar{b}}$, $P_T^{\gamma\gamma}$, $\eta_{\gamma\gamma}$, $\eta_{b\bar{b}}$, $M_{\gamma\gamma}$, $M_{b\bar{b}}$. Also the total invariant mass $M_{b\bar{b}\gamma\gamma}$ shows some differences in the large invariant mass region. The HEFT predictions for the distributions in $P_T^{b\bar{b}}$, $P_T^{\gamma\gamma}$, $\eta_{\gamma\gamma}$ and $\eta_{b\bar{b}}$ confirm the high transversality of these pairs, as expected from our previous comments on the high transversality of the two Higgs bosons produced. In the η distributions we see that central peaks at $\eta = 0$ in the red and green lines as opposed to the blue and black lines. In the case of the P_T distributions we see the long tails with small slopes at large transverse momentum. Finally, The HEFT predictions for the distributions in $M_{\gamma\gamma}$ and $M_{b\bar{b}}$ show clearly the peaks around m_H , as expected, in contrast to the broad distribution for the background (non-resonant) prediction. Any of these kinematic variables are therefore good candidates as signal/background discriminants. Accordingly, in the following we design new selections to improve the HH final state isolation that are based on the above behaviour found.

We define Selection **B** based on $M_{\gamma\gamma}$ and $M_{b\bar{b}}$ as follows:

Selection B $M_{\gamma\gamma}$ & $M_{b\bar{b}}$:

	SM E_i	$b\bar{b}\gamma\gamma jj$ BKG E_i
HH final state isolation	$120 < M_{\gamma\gamma} < 130$ GeV	55%
	$50 < M_{b\bar{b}} < 150$ GeV	89%
Total selection efficiency (A+B) ($\Pi^i E_i$)		18%
		1%

We define Selection **C** based on $\eta_{\gamma\gamma}$ as follows:

Selection C $\eta_{\gamma\gamma}$:

	SM E_i	$b\bar{b}\gamma\gamma jj$ BKG E_i
HH final state isolation	$-2 < \eta_{\gamma\gamma} < 2$	60%
Total selection efficiency (A+C) ($\Pi^i E_i$)		22%
		16%

Finally, we define Selection **C'** based on $P_{\gamma\gamma}^T$ as follows:

Selection C' $P_{\gamma\gamma}^T$:

	SM E_i	$b\bar{b}\gamma\gamma jj$ BKG E_i
HH final state isolation	$P_{\gamma\gamma}^t > 200$ GeV	8%
Total selection efficiency (A+C') ($\Pi^i E_i$)		3%
		1%

Then we propose two strategies, I and II, optimized for $\eta_{\gamma\gamma}$ and $P_{\gamma\gamma}^T$ respectively.

STRATEGY I (using $\eta_{\gamma\gamma}$) : Applies sequentially Selection A, Selection B and Selection C.

STRATEGY II (using $P_{\gamma\gamma}^T$) : Applies sequentially Selection A, Selection B and Selection C'.

The total number of ($b\bar{b}\gamma\gamma jj$) events expected at HL-LHC that are predicted for the HEFT models (with $-2 \leq a^2 - b \leq 2$), the SM (with $a=b=1$) and the dominant background, are summarized in the two tables 6 and 6, using Strategy I and Strategy II, respectively.

We learn from these tables, that both strategies are very efficient to discriminate between the HEFT signals and the background. The best one seems to be using the $P_{\gamma\gamma}^T$ cut at large transverse momentum (here, $P_{\gamma\gamma}^T > 200$ GeV). However this strategy if used with a too stringent cut may produce a rather poor signal statistics.

Finally, to complete our study we explore more values of the combination $a^2 - b = \kappa_V^2 - \kappa_{2V}$ and compute the expected sensitivity to this combination at HL-LHC for the two strategies I and II. For this computation we define the sensitivity S in terms of the number of signal events, N_S and background events N_B , as follows:

$$S = \sqrt{-2 \left((N_S + N_B) \log \left(\frac{N_B}{N_S + N_B} \right) + N_S \right)} \quad (6.1)$$

In Figs. 6.2 and 6.3 we show the predictions for S as a function of $\kappa_V^2 - \kappa_{2V}$ using Strategy I and Strategy II, respectively. In these (interpolated) predictions we have also explored the variations when moving κ_V and κ_{2V} separately within the ranges $0.95 < \kappa_V < 1.10$ and $-1 < \kappa_{2V} < 3$, for each fixed $\kappa_V^2 - \kappa_{2V}$ value within the range $-2 < \kappa_V^2 - \kappa_{2V} < 2$. These variations spread the predicted S parabolas a little bit producing the narrow colored bands.

STRATEGY I									
N	BKG	a =	1.10						
		b =	3.21	2.00	1.20	1.00	0.40	-0.30	-0.79
		a ² -b =	-2.00	-0.80	0.00	0.20	0.80	1.50	2.00
1)	VBF	690.70	69.07	9.43	1.58	3.87	20.29	58.65	97.67
2)	VBF + Eta	409.63	52.84	7.18	0.99	2.62	14.89	43.40	72.59
3)	VBF + M	19.80	18.96	2.49	0.75	1.58	6.71	18.30	31.63
4)	VBF + M + Eta	13.20	17.30	2.28	0.53	1.25	5.69	15.97	27.57

N	SM (a=b=1.00)	a =	0.95						
		b =	2.90	1.70	0.90	0.70	0.10	-0.60	-1.10
		a ² -b =	-2.00	-0.80	0.00	0.20	0.80	1.50	2.00
1)	VBF	1.02	76.30	10.56	0.78	2.50	17.55	55.10	92.93
2)	VBF + Eta	0.62	58.12	8.01	0.48	1.74	13.10	41.37	70.40
3)	VBF + M	0.50	21.85	2.74	0.37	0.96	5.99	16.94	28.88
4)	VBF + M + Eta	0.34	20.14	2.52	0.27	0.79	5.20	14.97	25.92

Table 6.3. Total number of ($b\bar{b}\gamma\gamma jj$) events expected at HL-LHC for the HEFT models (with $-2 \leq a^2 - b \leq 2$), the SM (with $a = b = 1$) and the dominant background, following Strategy I (using $\eta_{\gamma\gamma}$)

STRATEGY II

N	BKG	a =	1.10						
		b =	3.21	2.00	1.20	1.00	0.40	-0.30	-0.79
		$a^2 - b =$	-2.00	-0.80	0.00	0.20	0.80	1.50	2.00

1)	VBF	690.70		69.07	9.43	1.58	3.87	20.29	58.65	97.67
2)	VBF + M	19.80		18.96	2.49	0.75	1.58	6.71	18.30	31.63
3)	VBF + PT	17.60		18.41	2.56	0.13	0.57	4.13	13.01	23.27
4)	VBF + M + PT	0.24		11.86	1.70	0.09	0.38	2.80	8.42	15.95

N	SM (a=b=1.00)	a =	0.95						
		b =	2.90	1.70	0.90	0.70	0.10	-0.60	-1.10
		$a^2 - b =$	-2.00	-0.80	0.00	0.20	0.80	1.50	2.00

1)	VBF	1.02		76.30	10.56	0.78	2.50	17.55	55.10	92.93
2)	VBF + M	0.50		21.85	2.74	0.37	0.96	5.99	16.94	28.88
3)	VBF + PT	0.08		20.05	2.77	0.06	0.42	4.30	12.72	23.29
4)	VBF + M + PT	0.06		12.84	1.79	0.04	0.29	2.85	8.43	15.60

Table 6.4. Total number of $(b\bar{b}\gamma\gamma jj)$ events expected at HL-LHC for the HEFT models (with $-2 \leq a^2 - b \leq 2$), the SM (with $a = b = 1$) and the dominant background, following Strategy II (using $P_{\gamma\gamma}^T$)

From these two figures, 6.2 and 6.3, we learn that the expected sensitivity at HL-LHC to $\kappa_V^2 - \kappa_{2V}$ grows with the absolute value of this combination and reaches high values at the larger considered values in the interval (-2,2), for both strategies. In the case of Strategy I the maximum sensitivity reached is when applying the three selected cuts A+B+C, i.e. for $VBF+M_{\gamma\gamma,bb}+\eta_{\gamma\gamma}$. Concretely, we find $S = 4.9$ at $\kappa_V^2 - \kappa_{2V} = -2$ and $S = 6.4$ at $\kappa_V^2 - \kappa_{2V} = 2$. In the case of Strategy II we find even higher sensitivities than for Strategy I. The maximum sensitivity is reached when applying the three selected cuts A+B+C', i.e. for $VBF+M_{\gamma\gamma,bb}+P_{\gamma\gamma}^T$. Concretely, we find $S = 9.6$ at $\kappa_V^2 - \kappa_{2V} = -2$ and $S = 10.4$ at $\kappa_V^2 - \kappa_{2V} = 2$. The spread in the prediction of S due to varying separately κ_V and κ_{2V} for each value of the combination produces the colored bands but they are very narrow, indicating that for this study of $HHjj$ production at LHC the relevant parameter is not the separated κ 's but their combination $\kappa_V^2 - \kappa_{2V} = 2$, as we have said through all this work. Finally, these sensitivity plots also demonstrate that the decay products of the two final Higgs bosons, i.e. the $\gamma\gamma$ and $j_b j_b$ pairs inherit the high transversality of the two H's, and as a consequence, the use of differential distributions with variables like $\eta_{\gamma\gamma}$ and $P_{\gamma\gamma}^T$ as discriminants between the BSM signal and the background turns out to be very convenient.

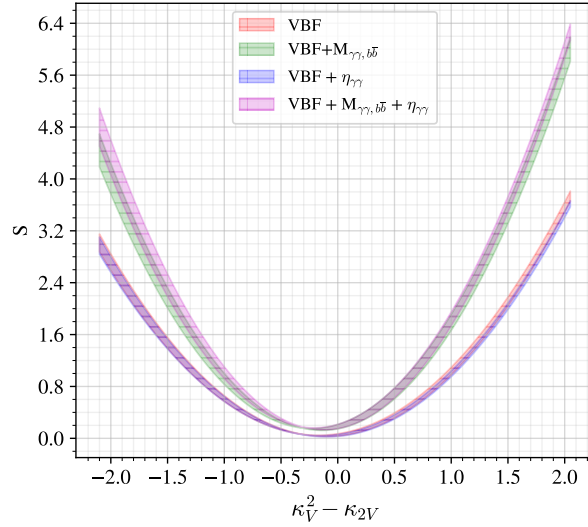


Figure 6.2. Predicted sensitivity to $\kappa_V^2 - \kappa_{2V}$ using Strategy I, based on $\eta_{\gamma\gamma}$. The results for the Selections, A (salmon) A+B (green), A+C (blue) and A+B+C (pink), are shown in different colors. The narrow colored bands along each parabola are produced when moving separately κ_V and κ_{2V} for each $\kappa_V^2 - \kappa_{2V}$ value.

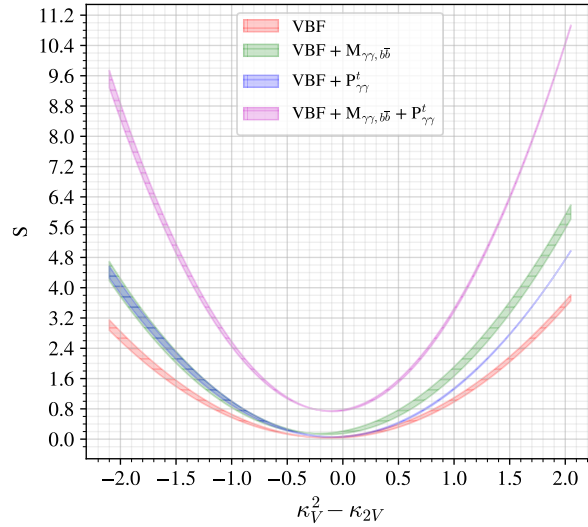


Figure 6.3. Predicted sensitivity to $\kappa_V^2 - \kappa_{2V}$ using Strategy II, based on $P_{\gamma\gamma}^T$. The results for the Selections, A (salmon) A+B (green), A+C' (blue) and A+B+C' (pink), are shown in different colors. The narrow colored bands along each parabola are produced when moving separately κ_V and κ_{2V} for each $\kappa_V^2 - \kappa_{2V}$ value.

Conclusions

In this work, we have studied the effective interactions HHV and $HHVV$ within the HEFT context and their potential correlations described by the combination parameter $a^2 - b = \kappa_V^2 - \kappa_{2V}$. We have selected the process $pp \rightarrow HHjj'$ at LHC, which is sensitive to this particular combination $\kappa_V^2 - \kappa_{2V}$, in contrast

to single Higgs production, which is only sensitive to κ_V . The interest in this particular combination of κ 's parameters is because it can give access to potential correlations between the HVV and $HHVV$ effective interactions that may occur in the low energy limit of the particular high energy fundamental theory, which is underlying the Higgs sector of the Electroweak Theory and the spontaneous symmetry breaking of $SU(2) \times U(1)$. The particular setting $\kappa_V = \kappa_{2V} = 1$ corresponds to the SM case, and therefore any deviation from this setting implies BSM Higgs Physics. We have used here as low energy theory the HEFT, which is a gauge invariant $SU(2) \times U(1)$ theory, allowing for a fully gauge invariant computation of all scattering amplitudes and cross sections of interest. Within the HEFT, these two effective coefficients, $a = \kappa_V$ and $b = \kappa_{2V}$, are treated as independent parameters and are generically uncorrelated parameters. It is in particular settings for the UV underlying theory, where, after integration of the heavy modes, the predictions for a , b and $a^2 - b$ could give rise to the mentioned correlations between the effective interactions HVV and $HHVV$ at low energies. Therefore, studying the potential correlations via the combination $\kappa_V^2 - \kappa_{2V}$ which we propose here could provide interesting signals of BSM Higgs physics.

Here we have first described, both analytically and numerically, how this combination $\kappa_V^2 - \kappa_{2V}$ appears at the subprocess level. This particular combination appears explicitly at large energies compared to the masses, in the scattering amplitude of double Higgs production from two longitudinal EW gauge bosons: $V_L V_L \rightarrow HH$ with $VV = WW$ and $VV = ZZ$. The particular behaviour at $\sqrt{s} \gg m_H, m_V$ of this dominant helicity amplitude growing with energy as $\mathcal{A} \sim (\kappa_V^2 - \kappa_{2V})s/v^2$ is the clue to understand the relevance of studying this combination.

We have then focused our study on the production of $HHjj$ at LHC which, with a properly designed strategy, may access directly to this combination. The strategy proposed here is to first make a selection of events having dominantly the so-called Vector Boson Fusion (VBF) topology, precisely because in this topology is where the $\kappa_V^2 - \kappa_{2V}$ combination governs the $HHjj$ event rates. Our study of $HHjj$ event rates with VBF topology within the HEFT models indicates that not only the total cross section $\sigma(pp \rightarrow HHjj)$ but also the differential cross sections like $d\sigma(pp \rightarrow HHjj)/d\eta_H$ are very sensitive to this $\kappa_V^2 - \kappa_{2V}$ combination. The total rates clearly grow with $\kappa_V^2 - \kappa_{2V}$, and the distributions with respect to the final Higgs boson pseudo-rapidity show a clear peak at central rapidity $\eta_H = 0$. This demonstrates that within these HEFT scenarios with $(\kappa_V^2 - \kappa_{2V}) \neq 0$ a good discriminant of BSM signals with respect to the SM rates will be to search for these central peaks indicating the high transversality of the Higgs produced, and in consequence also of its decays.

We have then fully studied the complete process, $pp \rightarrow HHjj' \rightarrow b\bar{b}\gamma jj'$, that includes the particular Higgs decays, $H \rightarrow b\bar{b}$ and $H \rightarrow \gamma\gamma$ which offer good prospects for the detection of BSM Higgs physics. We have analyzed the final state events, $b\bar{b}\gamma jj'$, with two light jets, two b-jets and two photons for both the HEFT signals, considering various values of the combination parameter, and for the dominant background, SM-QCD-EW (non-resonant), and we have taken into account in all cases the realistic effects from showering, clustering, hadronization and detector. To implement these effects, the parton-level $pp \rightarrow b\bar{b}\gamma jj'$ simulated events with MG5 are filtered to incorporate PYTHIA and DELPHES simulations, which account for showering and hadronization effects, as well as the jet clustering, and for a parametric simulation of the detector, in particular the future upgraded Phase-2 CMS detector. As a result of the excellent capabilities for photon and b-jet identification of the detector in the phase space regions of our interest, the HH relative sensitivities that allow us to discriminate between HEFT models with different values for the combination $\kappa_V^2 - \kappa_{2V}$ are preserved almost unchanged. In particular, the shapes of the distributions with respect to the pseudo-rapidity of H , translated to the pseudo-rapidity of the $\gamma\gamma$ pairs remain unchanged and show clearly the centrality and high transversality of these $\gamma\gamma$ pairs in the HEFT events as compared to the SM events. The Detector-level predictions deviate from parton-level

predictions almost exclusively by a general scale-down of the total rates, resulting from a prediction of the experimental acceptance and resolution of the process. We have shown that higher combined selection efficiency values are obtained from HEFT $HHjj$ signals with a greater $\kappa_V^2 - \kappa_{2V}$ combination value. We have also shown that HEFT $HHjj$ production involving a and b parameters with higher values for the $\kappa_V^2 - \kappa_{2V}$ combination leads to signals with greater detector-level efficiencies, i.e. smaller event loss with respect to the parton-level estimations, and a greater number of predicted events at the pp LHC experiments.

Finally, we have presented specific strategies focused on the choice of the proper variables and the proper cuts that lead to enhancing the sensitivity to the $\kappa_V^2 - \kappa_{2V}$ combination for the future HL-LHC operation. These proper variables have been extracted by studying the various relevant differential cross sections for signal and background. To enhance the signal versus background sensitivity, we have proposed two main routes. The two of them use first the $b\bar{b}\gamma jj'$ events selection by means of the important requirement of VBF topology. The two of them also use the HH final state isolation criteria based on $M_{\gamma\gamma}$, and $M_{b\bar{b}}$ being close to m_H . The main difference between the two strategies is the variable chosen for the study of the transversality of the final $\gamma\gamma$ and $b\bar{b}$ pairs. Strategy I uses mainly $\eta_{\gamma\gamma}$, and Strategy II uses mainly $P_{\gamma\gamma}^T$. Our final results in figures 6.2 and 6.3 show that both Strategies will provide efficient access to this $\kappa_V^2 - \kappa_{2V}$ combination and will lead to notable sensitivities to the largest values of this parameter, once the proper cuts for VBF+ $M_{\gamma\gamma, b\bar{b}} + \eta_{\gamma\gamma}$ or for VBF+ $M_{\gamma\gamma, b\bar{b}} + P_{\gamma\gamma}^T$, respectively, have been applied.

The general conclusion drawn from our work is that the BSM $HHjj$ signal strengths grow explicitly with the value of the $\kappa_V^2 - \kappa_{2V}$ combination within the considered HEFT models. This conclusion is preserved when considering the decay of both Higgs bosons, in particular for the $b\bar{b}\gamma\gamma$ decay channel, which offers good experimental prospects. It is also (nearly) independent of whether we include the showering, hadronization, and clustering effects and the parametric simulation of the detector. This is so because the event distributions with respect to the relevant variables, like $\eta_{\gamma\gamma}$ and $P_{\gamma\gamma}^T$, do not change appreciably when moving from parton-level to detector-level predictions. This leads to clear theoretical predictions and kinematic properties that can be translated into experimentally testable event characteristics within the projected HL-LHC operation and Phase-2 CMS detector, for which we expect to obtain the first evidence of the HH production. In the most pessimistic case that this future experimental search of BSM $HHjj$ production at HL-LHC does not find any deviation with respect to the SM predictions, our study indicates that improved constraints on BSM Higgs via the particular combination $\kappa_V^2 - \kappa_{2V}$ will be definitely set.

Acknowledgments

We wish to warmly thank Maria Cepeda for her valuable help in the evaluation of the efficiencies loss due to showering, hadronization, and detector effects, which have been simulated in the present work with PYTHIA and DELPHES. The results presented here would not have been possible without her guide and advice. We would also like to thank Michele Selvaggi for kindly providing us with the Snowmass21 Delphes card. Its use has been fundamental and has greatly contributed to the results of this work. We also warmly acknowledge the valuable help from Roberto Morales who participated in the building of the HEFT model file for MG5 which is used in this work. We acknowledge partial financial support by the Spanish Research Agency (Agencia Estatal de Investigación) through the grant with reference number PID2022-137127NB-I00 funded by MCIN/AEI/10.13039/501100011033/ FEDER, UE. We also thank financial

support from the grant IFT Centro de Excelencia Severo Ochoa with reference number CEX2020-001007-S funded by MCIN/AEI/10.13039/501100011033, from the previous AEI project PID2019-108892RB-I00 funded by MCIN/AEI/10.13039/501100011033, and from the European Union's Horizon 2020 research and innovation programme under the Marie Skłodowska-Curie grant agreement No 860881-HIDDeN. The work of D.D. is also supported by the Spanish Ministry of Science and Innovation via an FPU grant No FPU22/03485.

Appendices

A Feynman diagrams for double Higgs production in hadronic collisions

The present appendix summarizes the diagrams involved in calculating the Higgs boson pair production and two jets at hadron colliders, $pp \rightarrow HHjj'$. For brevity, only the partonic $q_1\bar{q}_2 \rightarrow HHq_3\bar{q}_4$ case is displayed here, but all the partonic cases with initial quarks and anti-quarks are included in the final computation. Notice also that only the diagrams with asterisk are of VBF topologies, whereas all the others are of associated production (double Higgs-strahlung) topologies, whose respective generic representations have been summarized in Figure 4.1. All the diagrams are obtained using MADGRAPH5 (MG5) [18] and the particular HEFT model defined in Refs. [9–12]

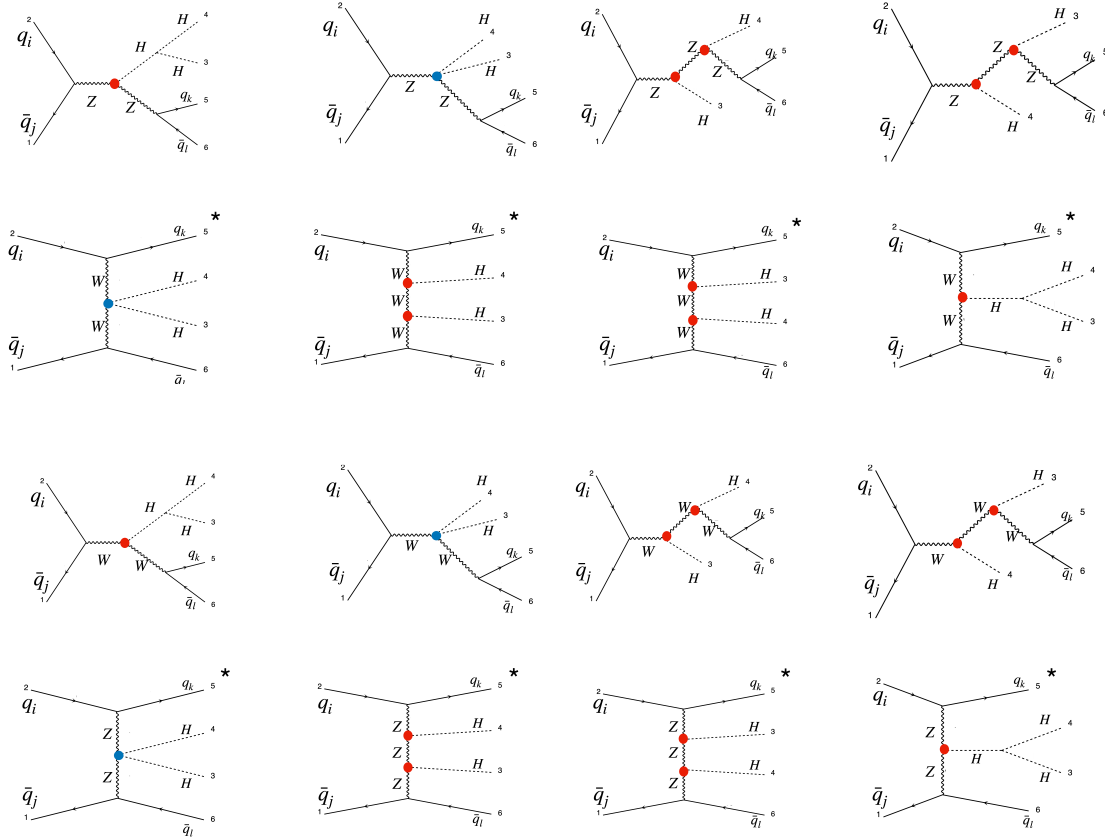


Figure A.1. Feynman diagrams for double Higgs production in proton-proton collisions. Diagram topologies marked with a * are also present in the MG5 calculus considering an q - q and \bar{q} - \bar{q} initial states. Remind that $q \equiv u, d, c, s$ and $\bar{q} \equiv \bar{u}, \bar{d}, \bar{c}, \bar{s}$.

References

- [1] J. R. Andersen *et al.* (LHC Higgs Cross Section Working Group), (2013), [10.5170/CERN-2013-004](#), [arXiv:1307.1347 \[hep-ph\]](#)
- [2] A. Dainese, M. Mangano, A. B. Meyer, A. Nisati, G. Salam, and M. A. Vesterinen, eds., *Report on the Physics at the HL-LHC, and Perspectives for the HE-LHC*, CERN Yellow Reports: Monographs, Vol. 7/2019 (CERN, Geneva, Switzerland, 2019)
- [3] CERN Yellow Rep. Monogr. **7**, Addendum (2019), [arXiv:1902.10229 \[hep-ex\]](#)
- [4] M. Cepeda *et al.*, CERN Yellow Rep. Monogr. **7**, 221 (2019), [arXiv:1902.00134 \[hep-ph\]](#)
- [5] M. Mlynarikova (ATLAS, CMS), in *30th International Workshop on Deep-Inelastic Scattering and Related Subjects* (2023) [arXiv:2307.07772 \[hep-ex\]](#)
- [6] ATLAS-CMS, “Highlights of the hl-lhc physics projections by atlas and cms,” (2025), [arXiv:2504.00672 \[hep-ex\]](#)
- [7] I. Brivio and M. Trott, *Phys. Rept.* **793**, 1 (2019), [arXiv:1706.08945 \[hep-ph\]](#)
- [8] A. Dobado and D. Espriu, (2019), [arXiv:1911.06844 \[hep-ph\]](#)
- [9] M. Herrero and R. A. Morales, *Phys. Rev. D* **102**, 075040 (2020)
- [10] M. J. Herrero and R. A. Morales, *Phys. Rev. D* **104**, 075013 (2021)
- [11] M. J. Herrero and R. A. Morales, *Phys. Rev. D* **106**, 073008 (2022)
- [12] D. Domenech, M. J. Herrero, R. A. Morales, and M. Ramos, *Phys. Rev. D* **106**, 115027 (2022)
- [13] D. Domenech, M. Herrero, R. A. Morales, and A. Salas-Bernárdez, (2025), [arXiv:2506.21716 \[hep-ph\]](#)
- [14] F. Arco, D. Domenech, M. J. Herrero, and R. A. Morales, *Phys. Rev. D* **108**, 095013 (2023), [arXiv:2307.15693 \[hep-ph\]](#)
- [15] J. M. Dávila, D. Domenech, M. J. Herrero, and R. A. Morales, *The European Physical Journal C* **84** (2024), [10.1140/epjc/s10052-024-12815-5](#)
- [16] M. Gonzalez-Lopez, M. J. Herrero, and P. Martinez-Suarez, *The European Physical Journal C* **81**, 260 (2021)
- [17] R. Contino, C. Grojean, M. Moretti, F. Piccinini, and R. Rattazzi, *Journal of High Energy Physics* **2010** (2010), [10.1007/jhep05\(2010\)089](#)
- [18] J. Alwall, R. Frederix, S. Frixione, V. Hirschi, F. Maltoni, O. Mattelaer, H.-S. Shao, T. Stelzer, P. Torrielli, and M. Zaro, *Journal of High Energy Physics* **2014** (2014), [10.1007/jhep07\(2014\)079](#)
- [19] T. Sjöstrand, S. Ask, J. R. Christiansen, R. Corke, N. Desai, P. Ilten, S. Mrenna, S. Prestel, C. O. Rasmussen, and P. Z. Skands, *Computer Physics Communications* **191**, 159 (2015)
- [20] J. de Favereau, C. Delaere, P. Demin, A. Giammanco, V. Lemaître, A. Mertens, M. Selvaggi, and T. D. . collaboration, *Journal of High Energy Physics* **2014**, 57 (2014)
- [21] M. Selvaggi, “Fcc-ee idea detector delphes card,” https://github.com/delphes/delphes/blob/master/cards/delphes_card_IDEA.tcl
- [22] R. D. Ball, V. Bertone, S. Carrazza, L. Del Debbio, S. Forte, A. Guffanti, N. P. Hartland, and J. Rojo, *Nuclear Physics B* **877**, 290 (2013), cited by: 440; All Open Access, Green Open Access
- [23] G. Aad *et al.* (ATLAS Collaboration), *Nature* **607**, 52 (2022)
- [24] G. Aad *et al.* (ATLAS Collaboration), *Phys. Rev. Lett.* **133**, 101801 (2024)
- [25] A. Tumasyan *et al.* (CMS Collaboration), *Nature* **607**, 60 (2022)
- [26] A. Hayrapetyan *et al.* (CMS), *Phys. Lett. B* **861**, 139210 (2025), [arXiv:2407.13554 \[hep-ex\]](#)

- [27] E. Arganda, C. Garcia-Garcia, and M. J. Herrero, [Nuclear Physics B](#) **945**, 114687 (2019)
- [28] J. M. Cornwall, D. N. Levin, and G. Tiktopoulos, [Phys. Rev. D](#) **10**, 1145 (1974), [Erratum: [Phys.Rev.D](#) **11**, 972 (1975)]
- [29] C. E. Vayonakis, [Lett. Nuovo Cim.](#) **17**, 383 (1976)
- [30] B. W. Lee, C. Quigg, and H. B. Thacker, [Phys. Rev. D](#) **16**, 1519 (1977)
- [31] R. L. Delgado, A. Dobado, and F. J. Llanes-Estrada, [Journal of High Energy Physics](#) **2014** (2014), [10.1007/jhep02\(2014\)121](#)
- [32] K. Doroba, J. Kalinowski, J. Kuczmarski, S. Pokorski, J. Rosiek, M. Szleper, and S. Tkaczyk, [Phys. Rev. D](#) **86**, 036011 (2012)
- [33] M. Szleper, “The higgs boson and the physics of ww scattering before and after higgs discovery,” (2015), [arXiv:1412.8367 \[hep-ph\]](#)
- [34] R. L. Delgado, A. Dobado, D. Espriu, C. Garcia-Garcia, M. J. Herrero, X. Marcano, and J. J. Sanz-Cillero, [Journal of High Energy Physics](#) **2017**, 98 (2017)
- [35] D. Gonçalves, T. Han, F. Kling, T. Plehn, and M. Takeuchi, [Physical Review D](#) **97** (2018), [10.1103/physrevd.97.113004](#)
- [36] F. A. Dreyer and A. Karlberg, [Phys. Rev. D](#) **98**, 114016 (2018)
- [37] M. Cacciari, G. P. Salam, and G. Soyez, [Journal of High Energy Physics](#) **2008**, 063 (2008)
- [38] M. Cacciari, G. P. Salam, and G. Soyez, [The European Physical Journal C](#) **72** (2012), [10.1140/epjc/s10052-012-1896-2](#)
- [39] CMS-PAS-FTR-18-019 (CMS Collaboration), (2018)
- [40] C. Collaboration (CMS), *Prospects for non-resonant Higgs boson pair production measurement in $bb\gamma\gamma$ final states in proton-proton collisions at $\sqrt{s} = 14$ TeV at the High-Luminosity LHC*, Tech. Rep. (CERN, Geneva, 2022)
- [41] S. Dawson, S. Dittmaier, and M. Spira, [Phys. Rev. D](#) **58**, 115012 (1998), [arXiv:hep-ph/9805244](#)
- [42] M. J. Dolan, C. Englert, N. Greiner, K. Nordstrom, and M. Spannowsky, [Eur. Phys. J. C](#) **75**, 387 (2015), [arXiv:1506.08008 \[hep-ph\]](#)